1-2021

A near-real-time approach for monitoring forest disturbance using Landsat time series: stochastic continuous change detection

Su Ye
Clark University

John Rogan
UC Santa Barbara, jrogan@clarku.edu

Zhe Zhu
University of Connecticut

J. Ronald Eastman
Clark University

Remote Sensing of Environment 252 (2021) 112167

Contents lists available at ScienceDirect

Remote Sensing of Environment

journal homepage: www.elsevier.com/locate/rse

A near-real-time approach for monitoring forest disturbance using Landsat time series: stochastic continuous change detection

Su Ye [a,*], John Rogan [a], Zhe Zhu [b], J. Ronald Eastman [c]

[a] Graduate School of Geography, Clark University, 950 Main Street, Worcester, MA 01610, USA
[b] Department of Natural Resources and the Environment, University of Connecticut, Storrs, CT 06269, USA
[c] Clark Labs, Clark University, Worcester, MA 01610, USA

ARTICLE INFO

Keywords:
Time series analysis
Forest disturbance
State space model
Kalman filter
Landsat
Near real-time

ABSTRACT

Forest disturbances greatly affect the ecological functioning of natural forests. Timely information regarding extent, timing and magnitude of forest disturbance events is crucial for effective disturbance management strategies. Yet, we still lack accurate, near-real-time and high-performance remote sensing tools for monitoring abrupt and subtle forest disturbances. This study presents a new approach called 'Stochastic Continuous Change Detection (S-CCD)' using a dense Landsat data time series. S-CCD improves upon the 'COntinuous monitoring of Land Disturbance (COLD)' approach by incorporating a mathematical tool called the 'state space model', which treats trends and seasonality as stochastic processes, allowing for modeling temporal dynamics of satellite observations in a recursive way. The quantitative accuracy assessment is evaluated based on 3782 Landsat-based disturbance reference plots (30 m) from a probability sampling distributed throughout the Conterminous United States. Validation results show that the overall accuracy (best F1 score) of S-CCD is 0.793 with 20% omission error and 21% commission error, slightly higher than that of COLD (0.789). Two disturbance sites respectively associated with wildfire and insect disturbances are used for qualitative map-based analysis. Both quantitative and qualitative analyses suggest that S-CCD achieves fewer omission errors than COLD for detecting those disturbances with subtle/gradual spectral change. In addition, S-CCD facilitates a better real-time monitoring, benefited by its complete recursive manner and a shorter lag for confirming disturbance than COLD (126 days vs. 166 days for alerting 50% disturbance events), and reached up to ~4.4 times speedup for computation. This research addresses the need for near-real-time monitoring and large-scale mapping of forest health and offers a new approach for operationally performing change detection tasks from dense Landsat-based time series.

1. Introduction

In the last two decades, linked to the recent elevated air temperature and prolonged drought, an increase in the occurrence and severity of forest disturbance has been documented over large parts of the globe (Dale et al., 2001; Seidl et al., 2017; Turner et al., 1998) for such as insect outbreak (Kautz et al., 2017; Paritsis and Veblen, 2011),wildfire (Pechony and Shindell, 2010; Westerling, 2016) and drought (Allen et al., 2015). Forest disturbance events directly emit carbon to the atmosphere through oxidation and decomposition of wood (Masek et al., 2008), and yield significant impacts on ecosystem services of national forests such as climate regulation and biological diversity conservation (Curran and Trigg, 2006). Therefore, it is important to systematically gather information regarding the extent, timing and magnitude of forest disturbance in an accurate and timely manner, enabling an early warning and effective management to prevent further loss of forested land (Rogan and Mietkiewicz, 2015).

For decades, satellite remote sensing has been promoted as a key data source for operational forest monitoring (Pasquarella et al., 2017). Particularly, the opening of the Landsat archive (Woodcock et al., 2008) has led to improved opportunities for characterizing forest disturbances from a long-term and consistent Landsat time series (Zhu, 2017). Compared to coarse-resolution datasets such as Moderate Resolution Imaging Spectroradiometer (MODIS, 250–1000 m resolution), Landsat-based time series are provided in a sufficient temporal length of 40-year global record of finer-resolution observations (30 m) (Masek et al., 2013). Therefore, Landsat data are often perceived as the best free-access remotely sensed data source for resolving the full range of

* Corresponding author.
E-mail address: sye@clarku.edu (S. Ye).

https://doi.org/10.1016/j.rse.2020.112167
Received 22 March 2020; Received in revised form 14 September 2020; Accepted 26 October 2020
Available online 5 November 2020

disturbance occurrence (Cohen et al., 2017; Cohen et al., 2016; Kennedy et al., 2014; Ye et al., 2018). Recently, the release of Landsat Analysis Ready Data (ARD) has eased automation for monitoring large-scale forest disturbances (Dwyer et al., 2018). The Landsat ARD gridded all available Landsat-4 and -5 TM, Landsat-7 ETM+ and Landsat-8 OLI/TIRS to an Albers Equal Area (AEA) Conic map projection, and are consistently geo-registered and atmospherically corrected, and hence holds the highest level of scientific standards and processing required for immediate use (Zhu, 2019). The Landsat ARD requires the minimum of user effort for data preprocessing, greatly facilitating a large-scale and long-term time series analyses (Dwyer et al., 2018).

A wealth of methodologies on satellite-based time series analysis have been developed for land cover change detection and characterization (Kennedy et al., 2010; Verbesselt et al., 2010a; Zhu and Woodcock, 2014b; Zhu et al., 2012). These approaches are often categorized based upon their monitoring strategies: offline or online monitoring (Bullock et al., 2019; Zhu, 2017). Offline monitoring focuses on a retrospective analysis when the collection of time series data is completed, and seeks to reconstruct forest disturbance history. The representative approaches for this category include LandTrendr (Kennedy et al., 2010), DBEST (Jamali et al., 2015) and the ensemble approach (Bullock et al., 2019). Online monitoring is applied to a practical scenario that the new observations are successively collected and processed in a timely fashion, and hence can be used for near real-time monitoring. Representative approaches for online monitoring are Breaks for Additive Season and Trend Monitor (BFAST Monitor) algorithm (Verbesselt et al., 2012) and Continuous Change Detection and Classification (CCDC) (Zhu and Woodcock, 2014b; Zhu et al. (2020)), though they are also applicable for offline monitoring. The BFAST was originally designed for temporal segmentation of MODIS-based time series (Verbesselt et al., 2010a), and was later modified (BFAST Monitor) to address near real-time detection for drought-related vegetation disturbance (Verbesselt et al., 2012). BFAST Monitor is a univariate approach that uses a single spectral band or index, while it has been reported that multiple bands or indices are more preferable because forest disturbance has a multi-spectral expression requiring multi-band inputs (Cohen et al., 2017; Zhu et al. (2020)).

CCDC is a multivariate time-series model that uses all available Landsat 4–8 data for change characterization and land cover classification (Zhu and Woodcock, 2014b). The CCDC first applies the Fmask (Zhu and Woodcock, 2012) and Tmask algorithm (Zhu and Woodcock, 2014a) to screen clouds, cloud shadows and snow, and then build a harmonic model for each spectral band based on remaining clear observations. A breakpoint indicative of the timing of the disturbance is identified when the minimum discrepancy between actual and predicted reflectance of spectral bands for a monitoring window is greater than a predefined change threshold (Zhu and Woodcock, 2014b). Recently, an improved algorithm called 'COntinuous Monitoring of Land Disturbance'(COLD) was developed based upon CCDC Zhu et al. (2020). COLD introduced several improvements such as disturbance extraction, temporally-adjusted Root Mean Square Error (RMSE), and change angles for disturbance confirmation Zhu et al. (2020). An important finding for COLD is that using the highest frequency for harmonic model updates, that is per observation instead of per a time span for the CCDC, can reduce ~20% commission errors Zhu et al. (2020). Zhu et al. (2020) tested the performance of COLD using 7200 Landsat time series plots randomly selected across the conterminous United States, and reported that the COLD algorithm achieves a higher accuracy than CCDC (~20% commission and ~ 82% omission, see (Cohen et al., 2017), with 27% omission and 28% commission error for a variety of land disturbance types.

However, while the COLD algorithm has achieved improved performance for change detection accuracy, there are several issues limiting its implementation for operational monitoring. First, COLD is computationally expensive: the original MATLAB software takes ~5000 computing hours for a Landsat ARD tile (1–3 thousand images) based on our tests. The high computational requirement imposes limits on the application of COLD for a wide range of scientific research, especially for a large-area mapping such as at a state or continental scale. The cause for the slow speed is due to the per observation updating approach Zhu et al. (2020). For example, if the time series of a single pixel has 500 clear observations, COLD needs to re-train the model using the 'Least Absolute Shrinkage and Selection Operator' (LASSO) algorithm for approximately 500 times to complete a detection for this pixel. Computational redundancies arise from reconstructing models from scratch for each new observation being added to the time series. Second, the former version of COLD, namely CCDC, was designed to detect abrupt land cover change, and is less helpful for detecting those disturbances that yield small to medium spectral change magnitude (Brown et al., 2019; Cohen et al., 2017; Zhu et al. (2020)). A possible reason provided is that CCDC identifies gradual changes as the slope in the harmonic regression model as opposed to attributing them to a change on a specific date (Bullock et al., 2019). Though this issue was alleviated by COLD, it has not been fully solved yet as evident by the only 60% producer accuracy for the disturbance category 'stress' Zhu et al. (2020). Third, within the current workflow of COLD, near real-time monitoring is not fully operational because: 1) COLD is a memory-intensive algorithm which requires loading all images to update model coefficients and to calculate temporally-adjusted RMSE for each new observation; 2) certain steps of COLD such as minimum RMSE require data inputs collected after the current monitoring date, which does not satisfy the need of near real-time monitoring. A recursive transformation for these steps can free the system from loading all historical images each time for a new observation, greatly improving computational efficiency for a near real-time scenario.

Currently, most operational near real-time products are based on MODIS system, such as Terra-i (Reymondin et al., 2012) and FORMA alert system (Hammer et al., 2014). To our knowledge, Global Land Analysis and Discovery (GLAD) is the only operational system providing a near real-time monitoring of forested land at a Landsat-pixel scale (Hansen et al., 2016). GLAD applies pre-trained decision trees models to classify clear observations and labels an alert if two or more out of four consecutive observations were classified into the disturbance category. As this product is designed and implemented only for tropical evergreen forest and no phenological variation is considered in the system (Hansen et al., 2016), its performance is unknown yet for those middle/high-latitude regions where disturbances signals are often spectrally similar to seasonal leaf drop.

In this study, we describe a new algorithm called 'Stochastic Continuous Change Detection' (S-CCD) that is developed to universally detect forest disturbance from Landsat time series in a recursive fashion. S-CCD introduces the state space theory into the current framework of COLD, aiming to address three objectives: 1) to enhance detection accuracy, especially for those forest change with small spectral change magnitudes while keeping a low rate for commission errors; 2) to provide an operational framework for near real-time monitoring; and 3) to improve computational efficiency, enabling a long-term time series analysis for a large-area forest disturbance characterization.

In what follows, we first provide an intuitive explanation for state space models and the Kalman filter as the mathematical foundation of S-CCD (Section 2), describe our S-CCD algorithm focusing on different steps with COLD (Section 3), introduce our reference dataset and validation metrics (Section 4) and exhibit the results for both quantitative and qualitative evaluation (Section 5), and finally discuss advantages and future work for S-CCD (Section 6). Of particular note is that Section 5.3 presents a high-performance software package for both S-CCD and COLD implemented in C language.

2. State space model and the Kalman filter

The new approach built upon the State Space Model (SSM), an established time-series mathematical framework that allows for

modeling a dynamic of observed measurements as being explained by a vector of latent state variables. The SSM has two foundational 'stochastic' assumptions: 1) observations are formulated as a sum of a stochastic item linked to the uncertainty within the data themselves, namely 'observational noise' (ϵ_t), and a vector of latent variables called 'states' (α_t); 2) states which are evolving over time as a stochastic process with being affected by a 'process noise' (η_t). Different from classical decomposition models such as harmonic regression used in BFAST and CCDC, SSM allows for trend and cycle components to be evolving randomly rather than deterministically (see Fig. 1), hence we called it as 'Stochastic Continuous Change Detection'.

The general Gaussian SSM can be written in the form as below (Durbin and Koopman, 2012):

$$\text{Observation equation}: y_t = Z\,a_t + \epsilon_t, \epsilon_t \sim N(0, H) \quad (1)$$

$$\text{State equation}: a_{t+1} = Ta_t + \eta_t, \eta_t \sim N(0, Q) \quad (2)$$

Where y_t is the observation at time t, ϵ_t and η_t are two mutually independent random variables that follow a normal distribution with mean 0 and variance H, and variance Q, respectively. Z is a system matrix in a binary form, which indicates those state items that directly contribute to the observation. T is a transformation matrix defining how a state vector evolves over time (mathematical definitions for Q, Z and T are detailed in the appendix). State space representation is central to statistical treatments for structural time series models, owing to its ability of allowing for structural components to be modeled explicitly by state variables (Brockwell and Davis, 2013; Durbin and Koopman, 2012). Therefore, SSM holds great promise for processing remote sensing time series, which are well known for the structure of 'trend + cycles' (Eastman et al., 2013; Verbesselt et al., 2010b; Zhu and Woodcock, 2014b).

The SSM for the state of 'trend' is formulated as a random-walk model:

$$\mu_{t+1} = \mu_t + \xi, \xi \sim N(0, \sigma_\xi^2) \quad (3)$$

Where ξ is a process noise item for the trend. The 'cycle' process requires two state variables to define:

$$c_{t+1} = c_t\, cos\, \lambda_c + c_t^*\, sin\, \lambda_c + \omega_t, \omega_t \sim N(0, \sigma_\omega^2) \quad (4)$$

$$c_{t+1}^* = -c_t\, sin\, \lambda_c + c_t^*\, cos\, \lambda_c + \omega_t^*, \omega_t^* \sim N(0, \sigma_{\omega^*}^2) \quad (5)$$

Where λ_c is the frequency of the cycle, ω_t and ω_t^* are independent process noise items. c_t is the primary cycle state, while c_t^* is an accessory state variable that is not included for prediction of y_t and only used to enable a recursive form of mathematical computation (so its corresponding element in Z is 0). For a classic model for 'trend + annual cycle + semi-annual cycle', the state vector a_t can therefore be given as $[\mu_t, c_{t,\,annual}, c_{t,\,annual}^*, c_{t,\,semi}, c_{t,\,semi}^*]$.

The Kalman filter is the most common tool providing an operational treatment for SSM. The Kalman filter was first developed for estimating real-time trajectory of the spacecraft for the Apollo program (Schmidt, 1981), and was later introduced to other application domains such as the control of linear systems (Davis and Vinter, 1985) and econometric modeling (Pasricha, 2006). Recently, the Kalman filter was applied to improve satellite-based time series analysis for applications such as crop phenology estimation (Vicente-Guijalba et al., 2014), synthetic NDVI image generation (Sedano et al., 2014) and near real-time monitoring of defoliation (Olsson et al., 2016). The Kalman filter is claimed to produce an optimal estimate in the sense that it always reaches the minimum mean square error, and is capable of predicting measurements in a recursive manner so that new measurements can be immediately processed as they arrive (Durbin and Koopman, 2012; Kalman, 1960). As such, the Kalman filter has great potential for being a fundamental tool of satellite-based near real-time monitoring.

Fig. 2 explains how the Kalman filter recursively adapts its model coefficients and prediction. When a new observation, '2000-12-27', is introduced into the time series, there is a discrepancy between the one-ahead-step prediction (the solid orange dot) and the new observation (the green cross) called 'innovation'. In a Kalman filter, the 'innovation' can be divided into two components: 1) observational noise; and 2)

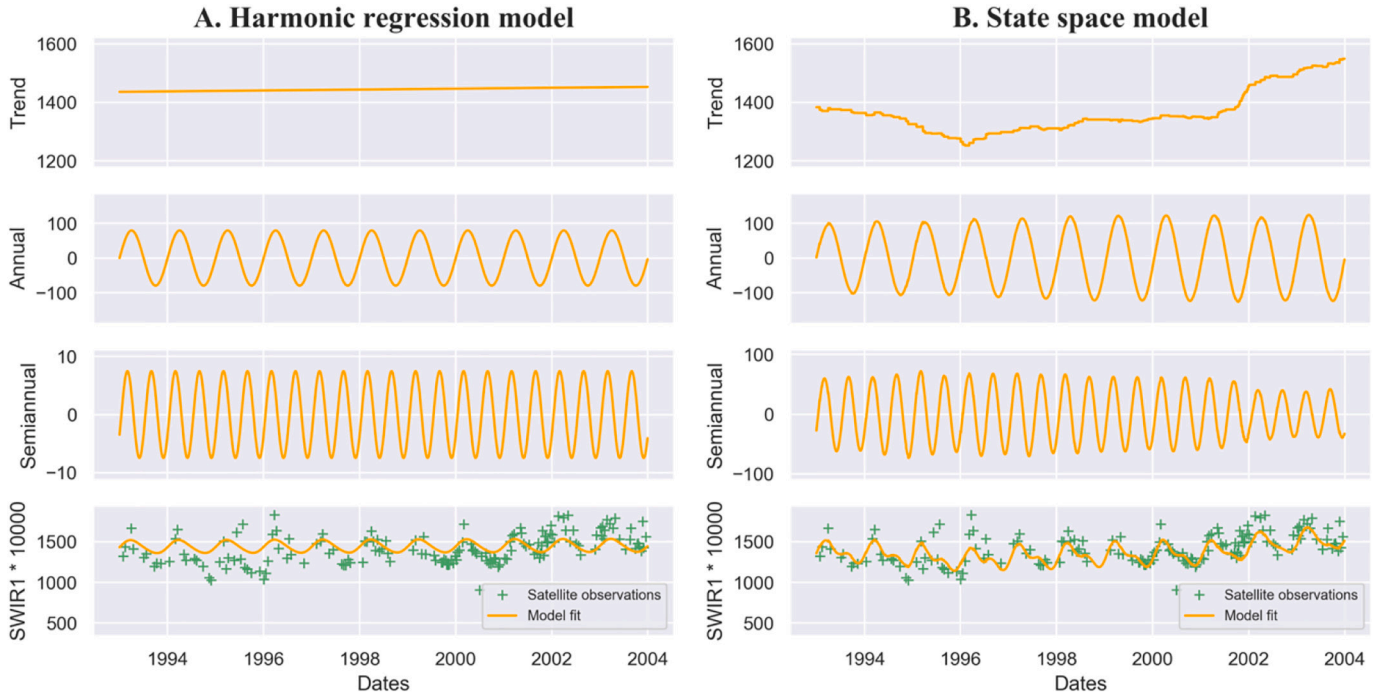

Fig. 1. The comparison between a harmonic regression model (A) and a state space model (B) for fitting curves. The harmonic regression model has a rigidity for consistent coefficients such as intercepts, slope and Fourier coefficients, while the state space model assumes that each component is evolving as a stochastic process so that the model coefficients vary over time.

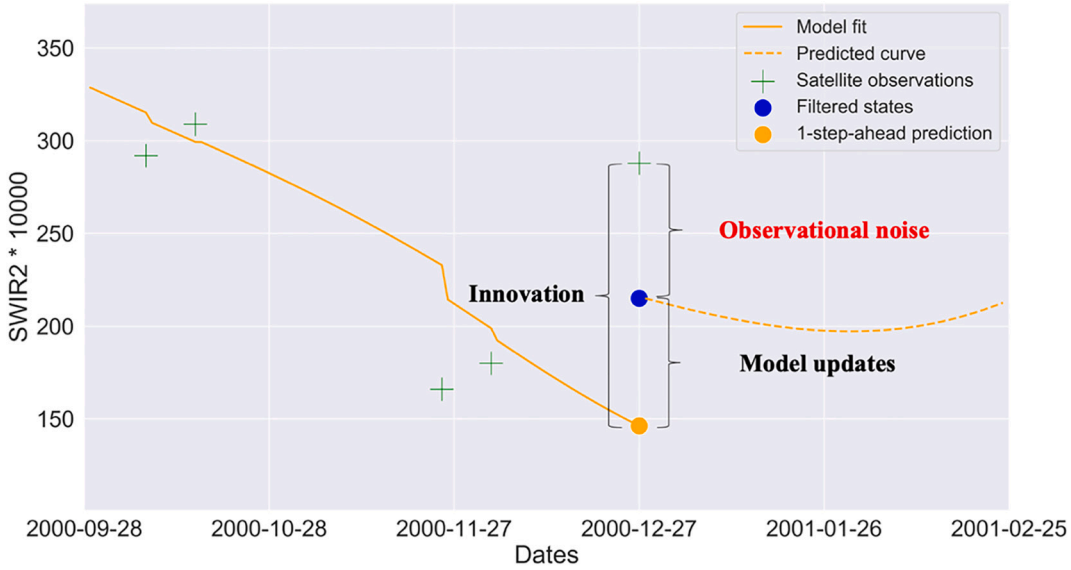

Fig. 2. An intuitive explanation of Kalman filter based on a Landsat time series. When a new observation at the date of '2000-12-27' is introduced to the system, the Kalman filter measures the difference between the actual observation (the green cross at '2000-12-27') and the predicted value (the green dot), namely 'innovation'. The fitting curve for the model will be adjusted to align with the optimal estimate for the current states (the 'blue dot') by filtering out 'observational noise' from 'innovation'. (For interpretation of the references to colour in this figure legend, the reader is referred to the web version of this article.)

model updates brought by the new observation. The Kalman gain is the relative weight assigned to actual model updates, which can be estimated by covariances of states and observational noise. Once the Kalman gain is computed, the Kalman filter will use it to filter out observational noise from the innovation. The new model coefficient can be then adjusted to align with the remaining part, namely 'filter states' (the blue dot), yielding a new fitting curve (the dashed orange line). The filtered states (or adjusted coefficients) will be used to predict the next observation.

Vegetation dynamics often exhibit a complex trend, which is not guaranteed to be adequately approximated by a single linear mode (Burkett et al., 2005; Zhao et al., 2019). The assumption for stochastically varying states for SSM and Kalman filters avoids the rigidity of classical decomposition that assumes the stationarity of linearity and seasonality, hence complex dynamics from time-series data are uncovered and more local fluctuations can be captured (Brockwell and Davis, 2013). The flexibility of dynamic modeling directly leads to better fitness of the model, and hence potentially increases the sensitivity of the model to subtle changes because change magnitudes are often calculated relative to measurement of model fitness such as Root Mean Square Error (RMSE). Other advantages of a state space analysis for satellite-based time series include: 1) simple mathematical treatment of missing data (shown in Appendix) which is critical for dealing with satellite-based time series known for its temporal irregularity; 2) explicit consideration for measurement uncertainties for the noisy nature of remote sensing data; 3) high computational efficiency due to its recursive form.

3. Method

The workflow of S-CCD, which consisted of data preparation, model initialization and continuous monitoring, is presented in Fig. 3. We used five spectral bands of surface reflectance products (green, red, NIR, SWIR1 and SWIR2) as the algorithm inputs because Zhu et al. (2020) reported that these five spectral inputs alone can achieve the best performance compared to being combined with vegetation indices. We applied the same steps as COLD for S-CCD for data preparation, for which we refer to Section 3.1.1 of Zhu et al. (2020).

3.1. Build initial model

After a clear time series is prepared by Fmask (Zhu and Woodcock, 2012), initialization model window and Tmask (Zhu and Woodcock, 2014a), S-CCD needs to seek a stable stage to define a statistical reference for change identification which adopts the stability test and 'looking back' procedure Zhu et al. (2020). The subtle modification for S-CCD is that we used 18 instead of 12 as the required minimum number of clear observations for an initialization window (i.e., the window defining a stable stage to initialize continuous modeling): our new approach assumes a fixed structure of 'trend + annual + semiannual' for a time series which can be equivalent to 6-coefficient harmonic model. The suggested minimum observation window for a LASSO regression is 'number of coefficients * 3', hence the minimum observation number is set as 18. The reason for using a 6-coefficients model instead of a tri-modal component (8-coefficient model) is discussed in Section 6.

3.2. State space model (SSM) initialization

In S-CCD, an additional step is needed to initialize the parameters and the structural elements for state space models before the continuous monitoring starts. The initial SSM parameters include observational noise (H), process noise (Q), initial states (a_0) and initial covariance (P_0).

The parameters H and Q are the two most important SSM parameters, representing the uncertainty level for observations and each stochastic process. They are often estimated by maximizing likelihood through a Quasi-Newton numerical searching algorithm in literature (Durbin and Koopman, 2012; Helske, 2016). However, after initial tests, we learned that the Quasi-Newton algorithm was inefficient for processing millions of pixel-based time series. To overcome the issue, we designed a fast method for estimating H and Q, and a new method for estimating a_0 and P_0 based upon initial LASSO regression (this fast procedure was detailed in Section S1 in the supplementary material).

3.3. Temporally adjusted peek window

Like all CCDC-like approaches, for each newly-collected clear observation, S-CCD compares predictions and actual observations based

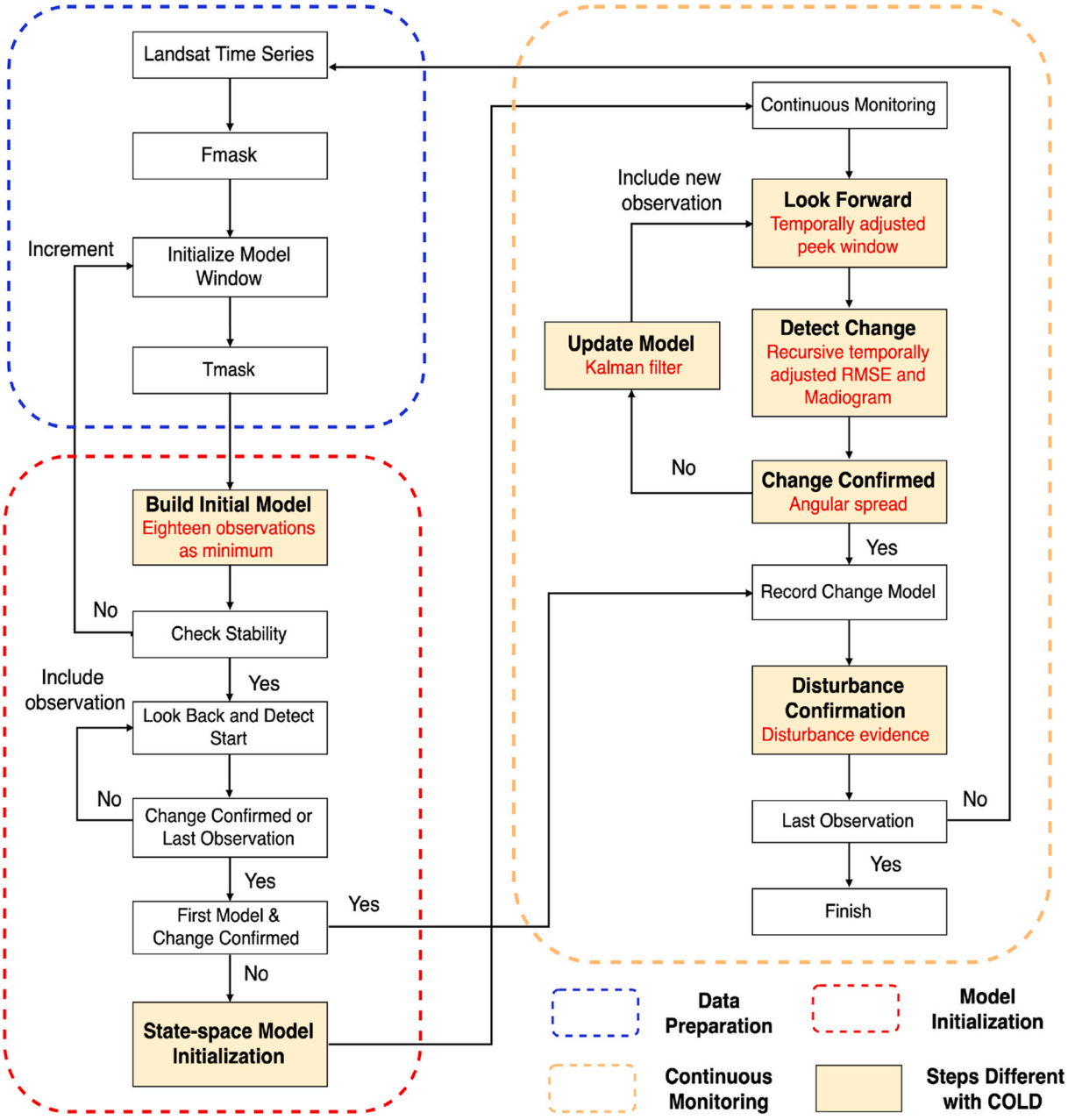

Fig. 3. The workflow of the proposed Stochastic Continuous Change Detection (S-CCD). Same as the original COntinuous Monitoring of Land Disturbance (COLD), the workflow consists of three stages: 1) data preparation, 2) model initialization, and 3) continuous monitoring. The different steps between S-CCD and COLD are highlighted as yellow polygons. (For interpretation of the references to colour in this figure legend, the reader is referred to the web version of this article.)

upon a number of consecutive anomaly observations, called the 'peek window' (Davis et al., 2017). COLD approach determines the number of consecutive observations via calculating the median revisit days across the entire time series. If the median revisit days are shorter than normal Landsat temporal density (16 days), more consecutive observations need to be included, and the probability threshold that all observations need to exceed is decreased to compensate Zhu et al. (2020). This approach requires an entire time series to compute median revisit days. We developed a completely online approach for adjusting the peek window for S-CCD. The number of observations for an temporally-adjusted peek window is defined as the minimum number satisfying 1) minimum consecutive observations, i.e., $conse_{def}$, and 2) the minimum temporal span for a peek window (*min_peek_days*):

$$conse_{def} = min\{x | \, x \geq conse_{def} \; and \; span(x) \geq min\_peek\_days\} \quad (6)$$

The defaulted consecutive number $conse_{def} = 6$. The *min_peek_days* is related to the temporal span for that a disturbance event can yield effects over the vegetation. If *min_peek_days* is set to be too long, signals of a disturbance might be affected by post-disturbance forest regrowth; if too short, some irrelevant ephemeral changes such as soil moisture change might be misidentified as disturbance. We explored the algorithm performance by using several *min_peek_days* below the normal peek window width (e.g. 60, 70, 80 days). Choosing *min_peek_days* as 80 days shows the best result (see Fig. S1 in the supplementary material). The threshold probability is also adjusted when a peek window chooses a consecutive observation number larger than $conse_{def}$, following Eq. S4 in Zhu et al. (2020).

Another advantage of the new peek window in terms of COLD approach is making it feasible to account for variability in Landsat observation frequency across not just space, but also time. Time series

segments collected in the early days (e.g. before the launch of Landsat 7 ETM+ on 1999) often have a lower temporal density than the most recent collections. Large changes in frequency driven by the number of active sensors aboard Landsat satellites had an influence on the CCDC/COLD change detection records (Brown et al., 2019): higher detection rates often occur at higher observation frequency particularly after the launch of Landsat 8 OLI, including commission errors brought by ephemeral forest change. The new peek window considers that the consecutive number is not fixed throughout the detection for a single time series and enables an adjustment of consecutive observations based upon the local temporal density for the peek window, because it defines the peek window according to the physical attribute of a disturbance signal, namely lasting days, not satellite observation count.

3.4. Recursive temporally-adjusted RMSE

Squared differences between predictions and observations are used to evaluate deviation of the current peek window from the 'stable stage'. RMSE is used to normalize the square difference, which is critical for decisions on the occurrence of breakpoints. Considering that RMSE often exhibits a yearly pattern over the whole time series (Zhu et al., 2015), the COLD algorithm employs a temporally-adjusted RMSE that is calculated based on the temporally closest 24 observations to the peek window. For operational near real-time monitoring, this temporally-adjusted RMSE needs to be re-computed by loading all images back into the model for a new observation. We designed a novel recursive method based upon two histograms respectively for clear observation counts (Fig. 4A) and square of RMSE (Fig. 4B) for Days of Year (DOY), which eliminates the need of processing all images for each new observation. Both histograms are defined as a bin width of 6 days, and 61 bins in total. The two histograms keep updating once a new observation is available. To compute a temporally-adjusted RMSE for a new observation, S-CCD will start from the bin at the middle date of the peek window ('Step 1' in Fig. 4A), and expand the searching window by an increment of one bin on the left and the right side each time, until the window includes $\geq$ 24 observations ('Step 3' in Fig. 4A). The temporal RMSE is computed as the average RMSE*RMSE of the resultant window based on the count and the temporal RMSE histogram.

Likewise, to enable near real-time monitoring, we used a dynamic minimum RMSE (or temporal lag-1 madogram), instead of a static minimum RMSE used in Zhu et al. (2020), to define the minimum value of RMSE for each band: the madogram is updated each year using all clear past observations.

Therefore, the new RMSE for S-CCD is computed as (b is bth Landsat band):

$$RMSE_b = max\left(recursive\_temporal\_RMSE_b, dynamic\_min\_RMSE_b \right) \quad (7)$$

For an observation n in a peek window, we define the Standardized Change Vector (SCV_n) as the difference between its multispectral reference and its one-step-ahead predictions relative to *RMSE* using the five bands (namely green, red, NIR, SWIR1 and SWIR2):

$$SCV_n = \left[\frac{y_{n,1} - \widehat{y}_{n,1}}{RMSE_1}, \frac{y_{n,2} - \widehat{y}_{n,2}}{RMSE_2}, \cdots \frac{y_{n,5} - \widehat{y}_{n,5}}{RMSE_5} \right] \quad (8)$$

Similar to the COLD algorithm, the change magnitude (*CM*) is used as the indicator of breakpoints, which is calculated as the minimum norm of SCV_n for a peek window. *CM* follows the Chi-squared distribution with k degree of freedom Zhu et al. (2020), where k is the number of the used spectral bands, namely '5'. A breakpoint candidate is identified if the *CM* meets the condition, where P refers to all observations within the peek window:

$$CM = \min_{n \in P} \left\{ \|SCV_n\|^2 \right\} \tilde{} \chi^2(k) > \chi^2_{threshold}(5) \quad (9)$$

3.5. Confirm change using angular spread

Ephemeral and systematic noise may also lead to relatively large change magnitudes for all observations within a peek window. The disturbance signal, however, should have a consistent change direction for multispectral surface reflectance bands. Therefore, the time series model needs to confirm the change from the consistency of change angles once the Chi-squared distribution test is passed. COLD confirms breaks using the mean included angle between pairs of neighboring change vectors smaller than 45 degrees. We found that this strategy is sensitive to outliers: for example, if there is an outlier in the six consecutive observations, two out of five neighbor pairs will be affected by this outlier (40% of the candidate angles); if there are two outliers in a peek window, more than half of neighbor pairs are biased. We designed a new change angle index called 'angular spread', referred as the angle between each standardized change vector for nth observation (SCV_n) and the median standardized change vector (*MedSCV*). The median change vector here is used to represent the average of the spectral response of a disturbance. Ideally, the observations for a disturbance should concentrate around the median change vector. We define 'Mean Angular Spread' for a peek window (Eq. 10) to represent the average angular departure of each candidate change vector to medium change vector. We compared the performance of the mean included angle as 45 degrees (the COLD approach) and the mean angular spread with 30, 45 degree. The best result is achieved by using mean angular spread as 30 degrees (Fig. S2 in the supplementary material). The advantage of 'Mean Angular Spread' is that is less sensitive to outliers existing in a peek window. For example, an outlier only affects a single change angle out of six angles for a default peek window (16.7% of the candidate angles).

$$Mean\ Angular\ Spread = \frac{1}{conse_{adj}} \sum_{n=1}^{conse_{adj}} \theta_{(SCV_n, MedSCV)} < 30^{\circ} \quad (10)$$

3.6. Update model using the Kalman filter

For those observations that are identified as being unchanged, non-consecutive outlier removal will be used with a change probability of 0.99999 (same as Zhu et al. (2020)). If the observation passes the outlier test, it will be inputted to the system to update the model using the Kalman filter (see the Appendix). Instead of rebuilding LASSO regression each time, the Kalman filter has an extremely simple mathematical treatment for updating models.

3.7. Disturbance identification

Breakpoints detected by the above procedure are not necessarily associated with forest disturbance, but maybe forest recovery. As the final step, we need to single out those breaks that are related to forest health decline led by disturbance. A typical forest disturbance will cause lower NIR, higher Red and higher SWIR values. Such spectral change, however, might be asynchronous. For example, when a forest is attacked by mountain pine beetle, the increase of SWIR often occurs first due to increased water stress, then is the increase of the red band, and finally the NIR band decreases owing to needle drop. Hence, we created an index called '*disturbance evidence*' (see Eq. 11) based on the medium Standardized Change Vector (*MedSCV*, defined in Section 3.5). '*Disturbance evidence*' aims to provide a combined analysis for multiple bands instead of a single band index. The breaks that are identified as being disturbance-related need to have a disturbance evidence larger than zero:

$$Disturbance\ evidence = MedSCV_{RED} - MedSCV_{NIR} + MedSCV_{SWIR1} > 0 \quad (11)$$

We compared '*Disturbance Evidence*' with COLD disturbance extraction with thresholds 0, −0.01, −0.02, and − 0.03. '*Disturbance Evidence*' had a higher F1 score than all other COLD disturbance extraction methods at

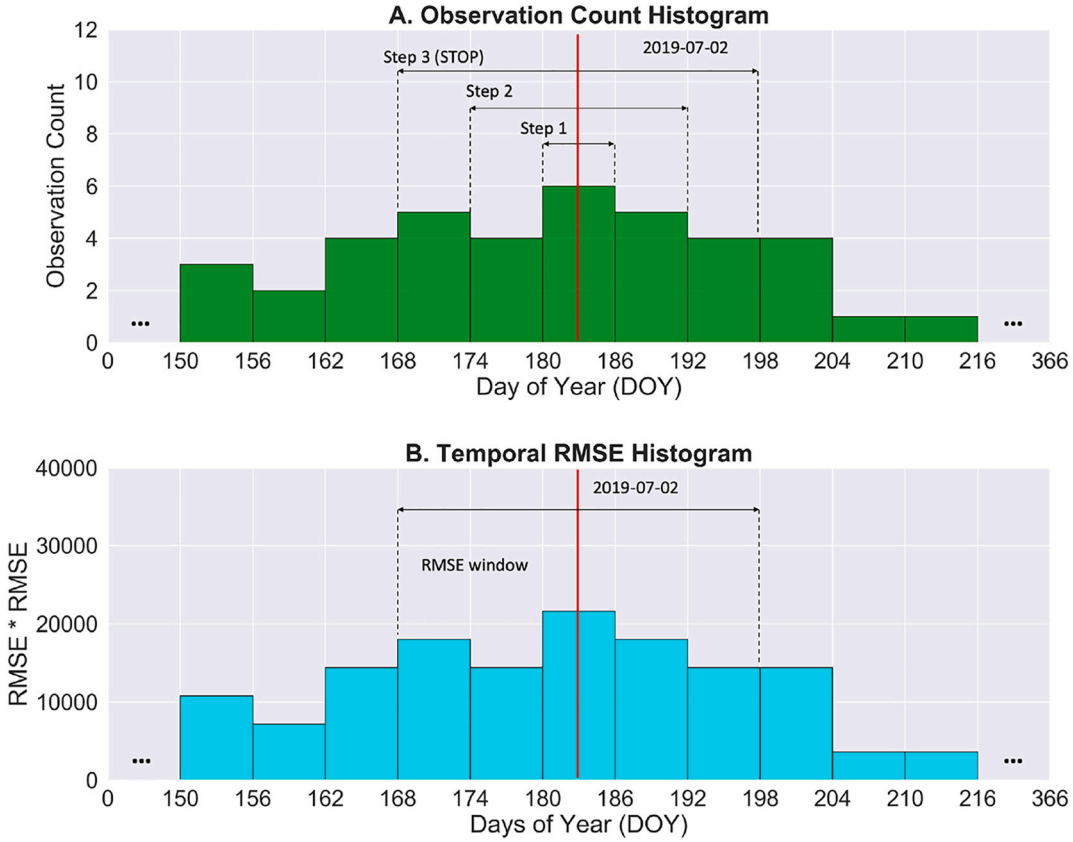

Fig. 4. The explanation for a recursive calculation of temporal RMSE: the algorithm searches a window that just covers ≥24 observations by an increment of a bin on both sides in an observational count histogram (Fig. 4A). Once it stops (Step3 in Fig. 4A), the temporal RMSE is computed as the average RMSE*RMSE within the resultant searching window.

all five thresholds (see Fig. S3 in the supplementary material).

3.8. Disturbance probability

For a scenario of near real-time monitoring, disturbance probability provides a fuzzy disturbance membership for a newly collected observation if the occurrence of a disturbance event has not been confirmed. Unlike GLAD (Hansen et al., 2016), COLD Zhu et al. (2020) and NRT-CCDC (Tang et al., 2020) which calculates a ratio of current consecutive anomaly observation count (i.e., the observations that has a change magnitude larger than the threshold) to the total required count, S-CCD computes disturbance probability as a ratio of 'anomaly days' to the required days for a confirmation (namely *min_peek_days*), given that the peek window in S-CCD is defined as natural days, not observation count. 'Anomaly days' is defined as the temporal span for current consecutive anomaly observations since the last 'stable' observation (as days). Disturbance probability have important implications for early management decision prior to statistically confirming a disturbance event, which will be discussed later in Section 5.3.

4. Study area, data and performance evaluation

Our performance evaluation for algorithms consisted of 1) quantitative accuracy assessment against a comprehensive national forest disturbance dataset, 2) qualitative evaluation based on large-scale assessment for two selected disturbance sites and 3) timeliness analysis for their near real-time implementation. For quantitative accuracy assessment, a benchmark forest disturbance database was chosen that includes 3782 Landsat-based forest plots across the conterminous United States (US) for which their disturbance timing and types have been well-interpreted from multiple data resources (Cohen et al., 2016; Zhu et al. (2020)). These forest plots were separated into 2704 undisturbed plots and 1078 disturbance plots with 1413 disturbance occurrences in total (some plots have successive disturbance occurrences such as fire and timber harvest). Among these disturbance occurrence, the most causal agent of disturbances is harvest (n = 903), followed by mechanical (n = 149), stress (n = 141), fire (n = 127), and others (n = 83, e.g., hydrology, wind, debris, land use change). For a detailed description of these disturbance causal agent classes, we refer to (Cohen et al., 2016). The spatial distribution of Landsat plots labeled as undisturbed or the number of disturbance occurrences is shown in Fig. 5. We randomly selected 50% of the reference samples (1891 Landsat plots) for algorithm development and parameter calibration. The other 50% of the reference samples were used as a holdout validation set to evaluate the comparative performance of S-CCD and COLD.

Considering that different algorithms may have different sensitivities to disturbance magnitudes based on change probability thresholds, the omission and commission rates based on a series of change probability, namely 0.90, 0.925, 0.95, 0.975, 0.99, were chosen for accuracy assessment. The overall performance is evaluated using the F1 score, because it provides a balanced assessment for omission and commission rates. The definition of omission, commission rates and F1 score are the same as Zhu et al. (2020).

$$F1\ score = 2*\frac{(1-commission)*(1-omission)}{2-commission-omission} \quad (12)$$

Qualitative map-based comparisons are performed to compare the performances of two algorithms for a large-area monitoring. We chose two Landsat ARD tiles that were respectively affected by fire and insect disturbance. The fire site sits at the San Juan and Rio Grande National Forests in southwestern Colorado, where Papoose fire burned 200 km^2 of forested in June and July 2013 (Verdin et al., 2013). The burned area

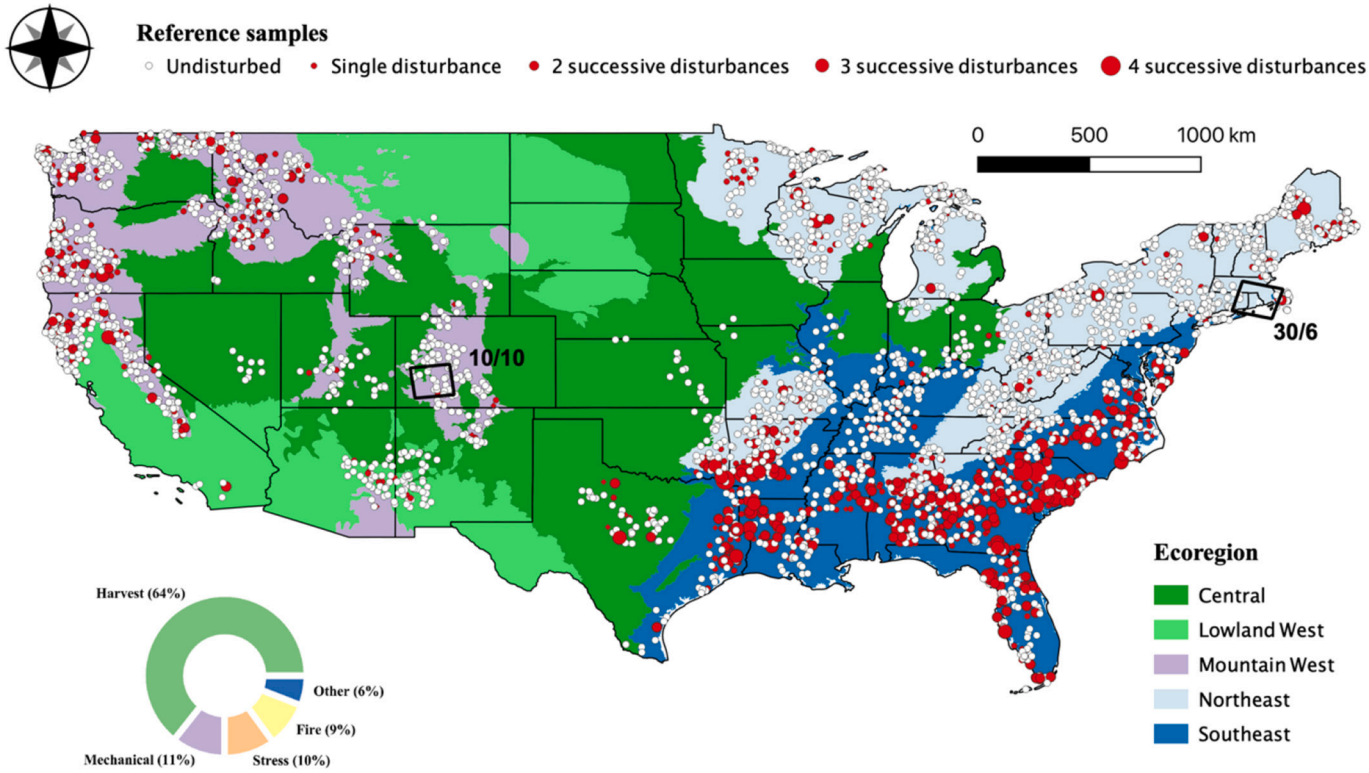

Fig. 5. The spatial distribution of 3782 reference sites, and two Landsat ARD scenes chosen as the study areas. The reference sites include 2704 undisturbed plots ('white circles') and 1078 disturbed plots (red circles), which were collected using a stratified sampling based on the ecoregions across the United States. There are 1413 disturbance occurrences in total, and the disturbance categories were dominated by the disturbance category 'Harvest' (63.9%), followed by 'Mechanical' (10.5%) and 'Stress' (9.9%). Landsat ARD 10/10 is located in the south Colorado including a region where Papoose fire happened in 2013; Landsat ARD 30/6 is located in the New England, including a site affected by gypsy moth infestation in 2016 and 2017.

was dominated by Engelmann spruce (*Picea engelmannii*) and Subalpine fir (*Abies lasiocarpa*) (Carlson et al., 2017). Caused by lightning, the Papoose fire starts on June 19, 2013, spread with a southeast direction, and was considerably dampened by precipitation on July 19, 2013 (Cyphers et al., 2019; United States Department of, 2014). All Landsat ARD images between 1996 and 2019 (25 years) were downloaded for analysis (ARD Tile Grid 10/10). A fire perimeter map for this specific fire provided by GeoMAC mapping application (https://rmgsc.cr.usgs.gov/outgoing/GeoMAC/) was used as our reference map. Directed by United States Geological Survey (USGS), GeoMAC updates the fire perimeter data based upon inputs from incident intelligence sources, GPS data, infrared imagery from satellite platform (Walters et al., 2011), and provides the most accurate perimeter map for this fire to our best knowledge.

The second disturbance site was chosen for gypsy moth (*Lymantria dispar*) infestation in Southern New England, which covers southern Massachusetts, northeast Connecticut, and northwest Rhode Island. This is a peri-urban region with 56.7% forest cover (i.e., 34.8% hardwood, 17.8% mixed and 4.1% conifer), and 26.7% developed area and 10.8% wetlands. This study area contains the locations that experienced from gypsy moth outbreak that started in 2015, spiked in 2017 (Pasquarella et al., 2018). A gypsy moth infestation can consume a large quantity of foliage and sometimes causes a near-total defoliation over a season or two (Townsend and Eshleman, 2004), but often starts to recover very soon for the following year, so the change signal is commonly ephemeral (Vogelmann et al., 2016). In addition, infested stands typically consist of two or more dominant tree species and are often represented by multi-aged and multi-sized populations (Hart and Veblen, 2015), making the detection all the more challenging because of mixed spectral response from various tree species. All Landsat ARD images for ARD Tile Grid 30/6 in recent 10 years (2010–2019) were downloaded and preprocessed. The Aerial Detection Survey (ADS) data[1] were used as reference dataset. The ADS data are polygon-based forest health maps from visually-defined polygons for a variety of specific insects and disease, annually reported by United States Department of Agriculture (USDA). It was reported that the recent ADS (after 2012) reached a high-level agreement to ground-collected reference data (4% omission and 5% commission for defoliation damage types) (Coleman et al., 2018). Generally speaking, in spite of its relatively coarse minimum mapping unit as 5 ha, the ADS data are a valuable source for indicating spatial distribution for forest disease at a broad scale (Hart and Veblen, 2015; Preisler et al., 2012) and the timing of disease occurrence, especially for the recent disturbances that occurred after 2012.

To evaluate the timeliness in a scenario of near real-time monitoring, we applied a metric called as "alert-lag relationship curve" (Tang et al., 2019). Like most time series algorithms, COLD and S-CCD both require a confirmation of a disturbance signal using consecutive observations, which may cause a lag for alerting disturbance in practice. We defined the alert lag as a delay between the beginning disturbance date and the date for confirming the disturbance. In practice, 'the beginning disturbance date' in this study was estimated as the first Landsat observation for a change signal of forest disturbance. Though the first Landsat observation signaling forest disturbance will not always coincide with the beginning of disturbance, they are the best resources for estimating the beginning disturbance date in a consistent way, given that reliable historical resources are often missing for disturbance-date response design. Due to that disturbance timings in our reference dataset were

[1] http://www.foresthealth.fs.usda.gov/portal/Flex/IDS

estimaed at an annual time step, we re-interpreted the beginning dates of the disturbances for randomly-selected 500 disturbance plots (~50% of the total disturbance plots, 665 disturbance events in total), based on a visualization of each plot-based Landsat time series. An alert-lag relationship curve was made based upon this date-level reference dataset to explore and compare disturbance detection rates, i.e., the proportion of confirmed reference disturbance events, at different lag times in a near real-time monitoring. In addition, disturbance probability maps, which can potentially provide timely information on disturbance progression and mitigating effects of detection latency, were outputted for timeliness analysis (see Section 5.3).

5. Results

5.1. Quantitative accuracy assessment

We tested COLD and S-CCD against a holdout validation set (n = 1891) using the different probability thresholds. The omission, commission and F1 score (see annotation around markers) for each test have been shown in Fig. 6A. S-CCD outperforms COLD at lower thresholds at 0.90, 0.925 and 0.95 for F1 score, while COLD is slightly better at higher thresholds at 0.975 and 0.99. The best accuracy they reached are close: S-CCD achieve the best performance as a F1 score of 0.793 (0.95 threshold probability, 20.1% omission and 21.4% commission errors), while COLD reaches the best accuracy as F1 score of 0.789 (0.975 threshold probability, 24.6% omission and 17.2% commission errors).

We also evaluated the performance of S-CCD and COLD against seven forest disturbance categories with a threshold probability of 0.95 (Fig. 6B). As Fig. 6B shows, S-CCD and COLD have very close omission errors for 'Harvest', 'Mechanical' and 'Wind'; S-CCD achieved lower omission error rate in the disturbance category 'Stress' and 'Fire', but is worse in 'Hydrology' and 'Other'. Surprisingly, the two approaches both have relatively high omission errors for 'fire' disturbance, which is often known for causing large change magnitude from satellite images (Cohen et al., 2016). The possible explanation can relate to some low-severity/underground fire cases are included in the reference dataset, which caused only subtle spectral change magnitude.

5.2. Qualitative analysis

For qualitative comparison, S-CCD and COLD were implemented to detect timing of forest disturbances respectively for Papoose fire and gypsy moth infestation. A consistent probability threshold as 0.95 was applied for both algorithms.

Fig. 7 illustrates the detection results of S-CCD and COLD for the Papoose fire site. Visually, COLD and S-CCD exhibit very similar detection results for abrupt disturbance categories such as moderate/high-severity fire. Given that this region was heavily affected by spruce beetle since 2010 (Hart and Veblen, 2015), we selected the breakpoints only detected in 2013, which is the year for Papoose fire occurrence, with an assumption that most of these breakpoints are associated with the fire, not spruce beetle attack for that year. To assess accuracy of timings for these breakpoints, we outputted month maps for the breakpoints detected in 2013. The breakpoints as detected mostly occurred in June and July (see Fig. 7A and B), which are well matched with the active temporal window of Papoose fire on the historical records (Cyphers et al., 2019). To further evaluate spatial accuracy for damage mapping, we compare two detection maps with GeoMAC fire perimeter map. GeoMAC contains some commission errors for mapping fire damage areas that are actually bare lands from High-resolution Satellite imagery, while COLD and S-CCD both accurately labeled them as 'no-attack' (see the example of Fig. 7D, E and F). It is noteworthy that Landsat 7 related scan-line corrector (SLC) artifacts can be both seen in the two breakpoint month maps, where SLC-off issue caused breakpoint dates to be several days to two weeks later (rounded to a month difference in our maps).

For the gypsy moth scene (Fig. 8), we compared years of breakpoints detected with Aerial Surveying Detection (ADS) data. Most disturbance events detected by COLD and S-CCD were concentrated at the deciduous forest cover regions of the 2016 NLCD map. The disturbance years indicated by two algorithms matched that of the ADS data (primarily the year of 2016 and 2017). This finding is consistent with the historical record that a major outbreak began in early summer 2016, led by a series of unusually dry springs (2014–2016) (Pasquarella et al., 2017). Admittedly, both algorithms yield much fewer affected regions than that

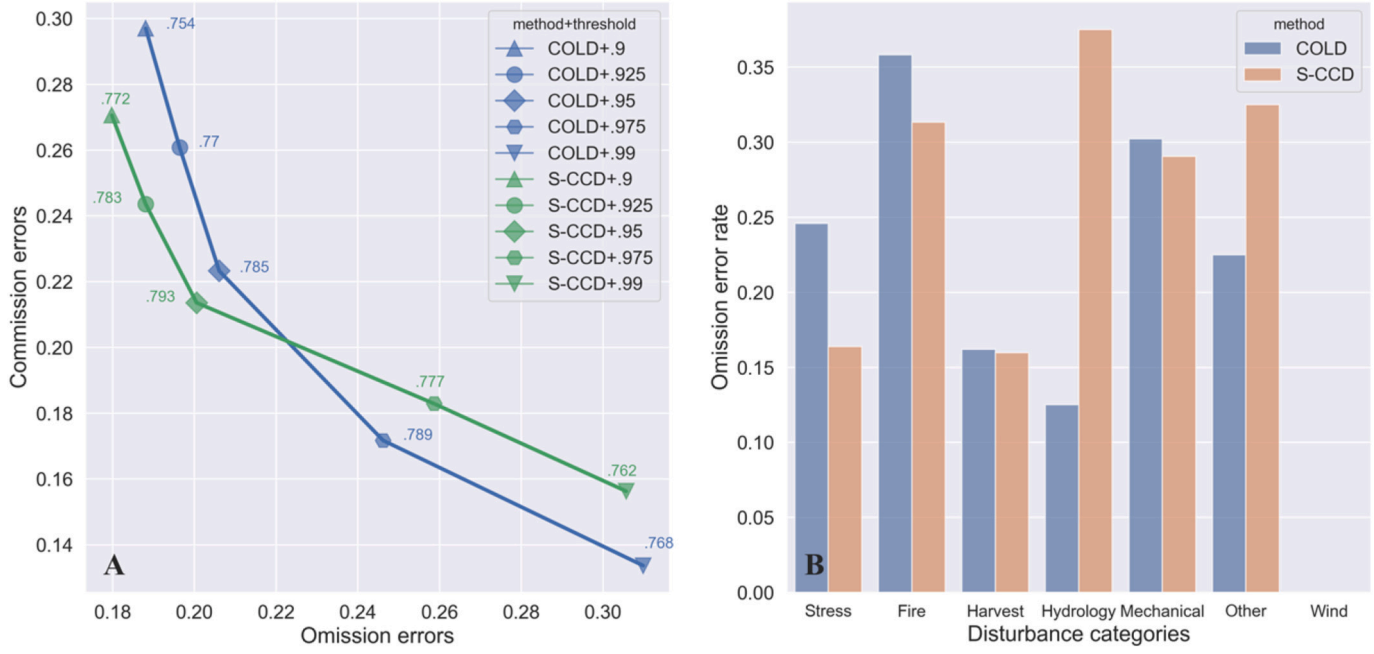

Fig. 6. Quantitative accuracy assessment results of COLD and S-CCD based on a holdout reference sample set (n = 1891). A) depicts omission, commission errors using a series of probability thresholds as 0.9, 0.925, 0.95, 0.975 and 0.99. The F1 score is used to evaluate the overall accuracy combining omission and commission errors, annotated around each marker. B) reports the omission errors of COLD and S-CCD for each disturbance category (note that the extremely low error rate for 'Wind' is due to that its samples number (n = 13) is too small).

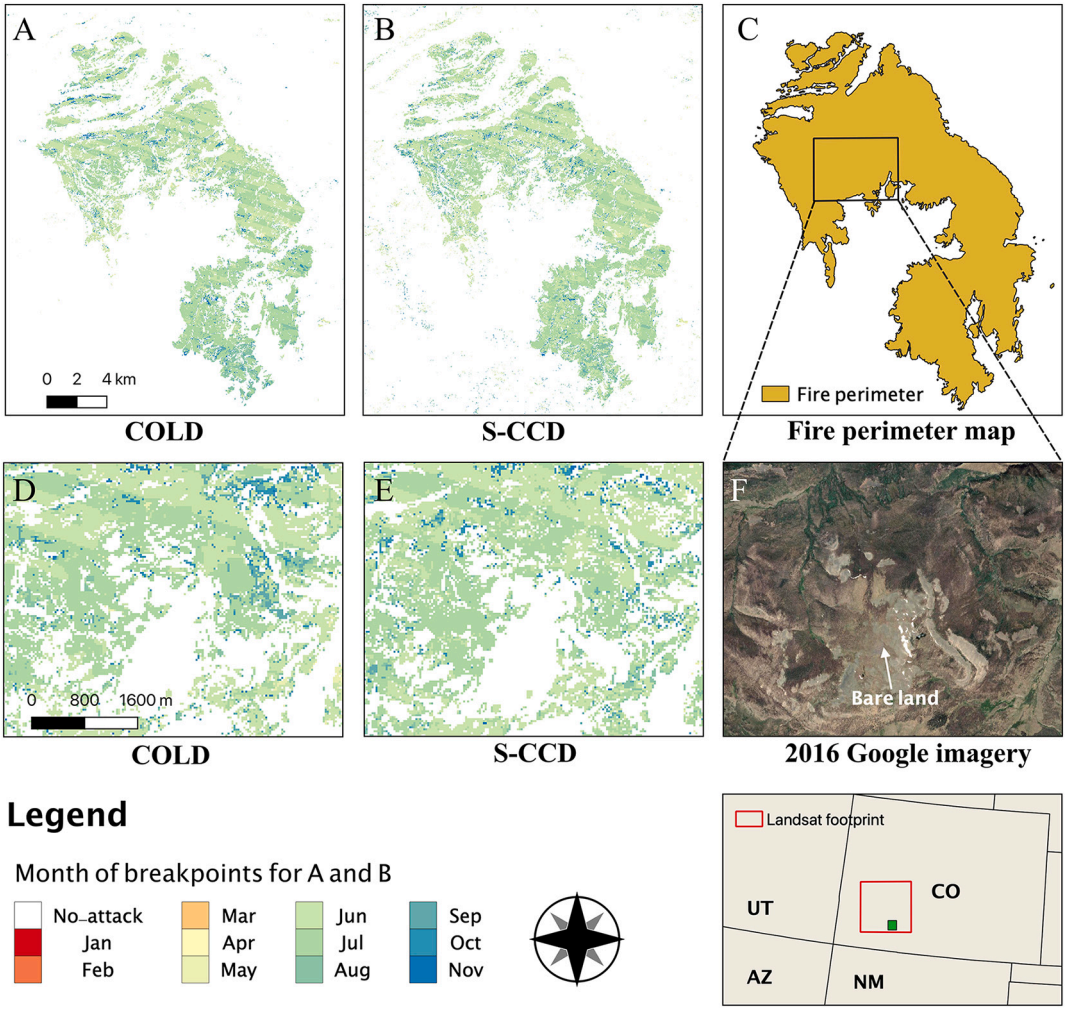

Fig. 7. Qualitative comparison for Papoose fire site (Landsat ARD 10/10) in Southeast Colorado among COLD (A), S-CCD (B) and GeoMAC fire perimeter map (C). COLD and S-CCD both use the probability threshold as 0.95. The colour for A) and B) denotes the month of breakpoints detected in 2013: the spectrum ranging from red to blue corresponds to months of breakpoints from January to November; the white are no-attack regions in 2013. D), E) and F) shows an example region that COLD and S-CCD both accurately delineated a non-attack bare land while GeoMAC over-detected it as fire region. (For interpretation of the references to colour in this figure legend, the reader is referred to the web version of this article.)

the ADS. Considering that Pasquarella et al. (2017) got the same result for their study in the Southern New England region, those omission errors might be due to commission errors in aerial sketch mapping. For comparative analysis, we found that COLD missed some regions affected by gypsy moth (e.g., the dashed blue circle in Fig. 8A), where S-CCD identifies most parts of the same region as forest disturbance. The locations and the disturbance years for extra regions detected by S-CCD have a general agreement with the ADS data (see the dashed circle in Fig. 8C), proving that these extra breakpoints detected by S-CCD for this region are related to forest damage caused by gypsy moth. We further visualized time series of NIR band for a sample pixel that COLD and S-CCD got conflicted detection results (Fig. 8F and G), and identified an occurrence of forest disturbance signal associated with a significant drop of NIR band within the temporal window of gypsy moth attack, and hence confirmed that the extra breakpoints detected by S-CCD were not commission errors.

5.3. Timeliness analysis

Fig. 9 depicts the alert-lag relationship curve which indicates the general latency between reference disturbance occurrence dates and confirmation dates of the algorithms based on 500 date-level reference plots. The steeper the curve appears to be, the fewer lag time that the algorithm requires to confirm the occurrence of a disturbance. Generally, S-CCD exhibits higher detection rates of disturbance than COLD given the same lag day (steeper curve), indicating that it is practically faster for alerting disturbance for a scenario of near real-time monitoring; S-CCD requires 126 days to confirm 50% of the disturbances (namely 50% detection rate) while COLD needs 166 days. Both curves plateaued at a detection rate of ~75%, which were caused by that the two algorithms missed detection for a proportion of reference breakpoints. To compare with other MODIS-based near real-time algorithms, S-CCD requires the same days (i.e., 126 days) to achieve 50% detection rates as NRT-CCDC which uses daily MODIS observations, but longer than the days required by Fusion 2 (i.e., 82 days) which combines Landsat and MODIS daily observations for a disturbance detection (Tang et al., 2019).

Fig. 10 shows a gradient of disturbance probabilities for an example of gypsy-moth-affected stand over a span of ~90 days since the first disturbance signals were detected. Fig. 10 A) are the breakpoint dates reported by a complete S-CCD, which shows that gypsy-moth attack occurs mostly at the dates 6-2-2016 and 6-18-2016 for this region. Fig. 10 B) – E) shows an increasing trend of disturbance probabilities with time going by: the region generally reached over a probability of 0.5 over 30 days since the initial infestation signal (Fig. 10 C); a proportion of disturbance pixels were confirmed (see 'light blue' pixels)

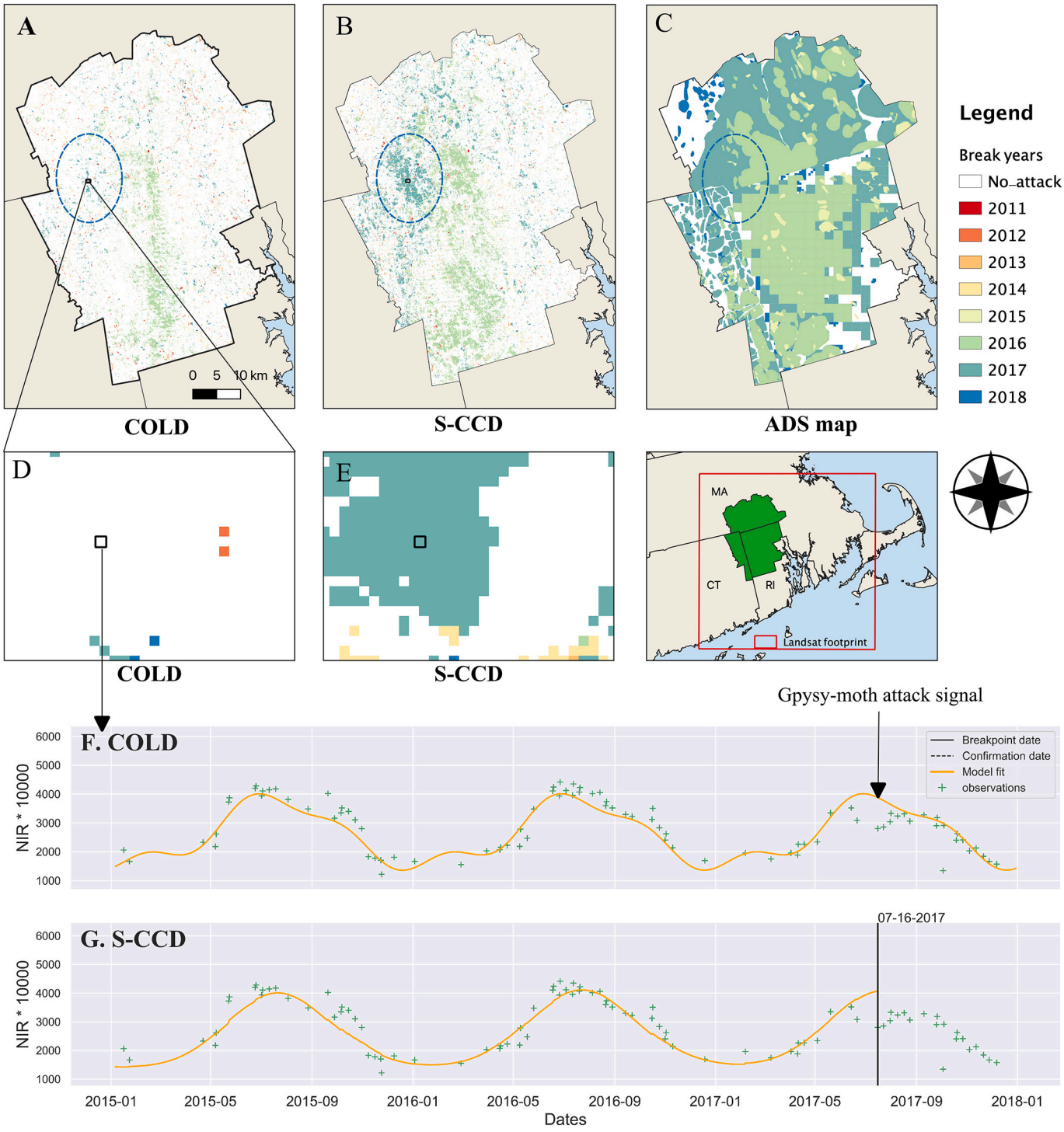

Fig. 8. Qualitative comparison for gypsy moth site (Landsat ARD 30/6) in Southern New England among COLD (A), S-CCD (B) and the ADS reference map (C). COLD and S-CCD both use the probability threshold as 0.95. The colour for (A), (B) and (C) denote the disturbance year indicated by each data source: the spectrum ranging from red to blue corresponds to the years from 2011 to 2018. Fig. 8 D) and E) show an example region that S-CCD can detected out the region that COLD missed gypsy moth damage. Fig. 8 F) and G) plots NIR time series of a sample pixel positioned at 'black rectangle' in D) and E) to confirm the occurrence of forest disturbance for this region. (For interpretation of the references to colour in this figure legend, the reader is referred to the web version of this article.)

over 60 days (Fig. 10 D); most disturbance pixels got confirmed after 90 days (Fig. 10E). The result illustrates that the temporal span of a disturbance signal can be continuously indicated by disturbance probabilities, which allows managers to choose thresholds based on practical needs. For example, a gypsy moth-affected region can be potentially determined by using a low alerting threshold (< 0.5) combined with spatial homogeneity analysis within 30-45 days since its initial symptom from Landsat time series, which can help locate early infestation and mitigate population expansion during its active window.

5.4. *Efficiency test and software implementation*

We implemented COLD and S-CCD in the high-performance C programming language. The C package named 'S-CCD' is downloadable

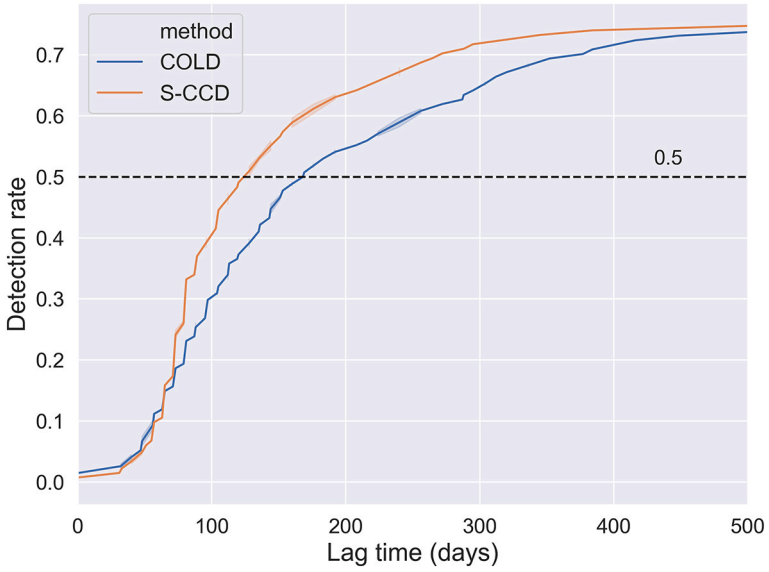

Fig. 9. The alert-lag table illustrating detection rates as a function of lag time based on 500 date-level reference disturbance plots.

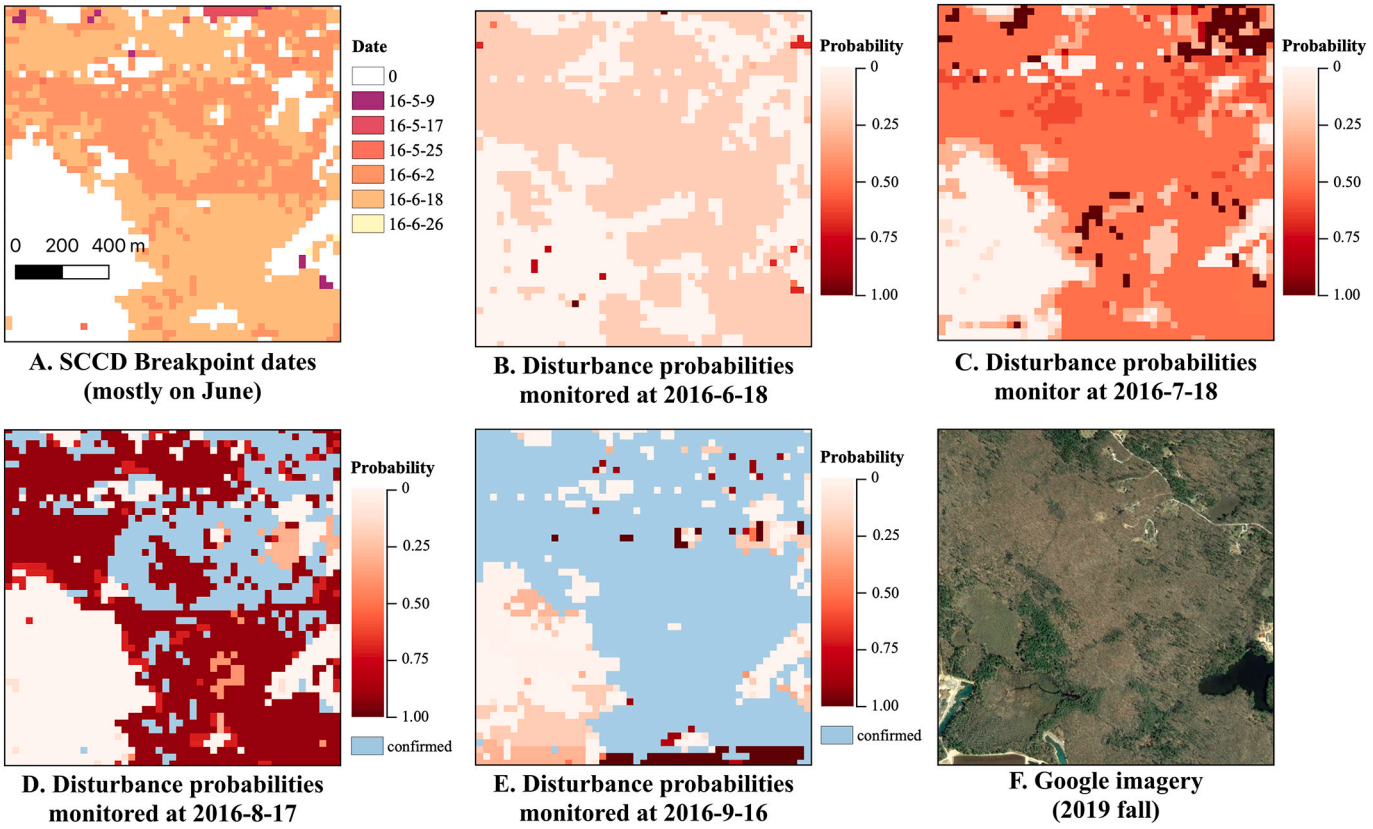

Fig. 10. An example of disturbance probability maps indicating disturbance progression for the near real-time monitoring. A) are the breakpoint dates from a complete detection S-CCD for a forest stand attacked by gypsy moth on June 2016; B) – E) shows a dynamics of disturbance probabilities (represented as red colour ramp) and confirmed disturbance pixels (light blue) every 30 days since initial attack. F) the reference high-resolution Google imagery. (For interpretation of the references to colour in this figure legend, the reader is referred to the web version of this article.)

from https://github.com/SuYe99/s-ccd. The software implemented a shared memory parallelization for COLD and S-CCD under a Linux/MacOS desktop environment, and has been already adapted for a High-Performance Computing (HPC) environment. It is noteworthy that our C-based COLD has been 1.5-2.0 times faster than the original MATLAB-based implementation.

To test the efficiency for C-based COLD and S-CCD, we used a 'dummy' Landsat ARD scanline which is a standard sample set of 5000 pixel-based time series plots selected from our reference sample set. The sample set consists of 3782 forest plots and 1218 non-forest plots. To uncover the effects of monitoring span on the speed, we pruned each time series into three different lengths of time series records, that is 10

years (2008–2017), 20 years (1998–2017) and 34 years (1984–2017). The results are summarized in Fig. 11. S-CCD can achieve up to ~4.4 times faster than the C-based COLD (with 34-year time series records). With the length of records decreasing, the efficiency improvement of S-CCD over COLD declines, as ~3.5 times at 20-year time series records, and ~ 1.8 time faster at 10-year time series records. This is because S-CCD improves efficiency mainly at the step of the model update; a longer time series needs a greater number for model updates to complete a detection, and hence more significant efficiency improvement made by S-CCD. For a standard 20-year Landsat ARD time series, our S-CCD program takes only ~6 min to finish a detection for a 5000-pixel scanline, and ~ 500 computing hours for a Landsat ARD scene.

6. Discussion

The quantitative accuracy assessment indicates that the differences between the best overall accuracy achieved by S-CCD and COLD are only 0.4% (see Fig. 6A, 0.793 v.s. 0.789). The primary reason is that our plot database is generated from random sampling over a nation-wide region, for which 63% of the forest disturbances are harvesting activities; the two approaches have very similar performance for detecting strong spectral signals yielded by those disturbances with medium- or high-severity and homogeneous tree damages such as harvest disturbances (omission errors: 16% v.s. 16.2%). Our map-based evaluation for Papoose fire case supports this conclusion.

S-CCD, however, achieved noticeably fewer omission errors than COLD for those lower-magnitude disturbances such as drought stress and low-severity fire (see Fig. 6b). This finding was confirmed by our qualitative comparison for the case study of gypsy moths. The reason could be that S-CCD allows for known changes in the structure of the system over time, and often can achieve a better model fitting than COLD that assumes the rigidity of "linear trend + harmonic cycles". We calculated the average RMSE for each band using all our 3782 samples. The results, as shown in Table 1, indicate that S-CCD has generally lower average RMSE than COLD for all seven spectral bands other than NIR and thermal bands (thermal band is not used to compute change magnitudes for both approaches, and thereby has no effects on break detection). As the two approaches both evaluated change magnitude relative to the RMSE, the lower RMSE means that S-CCD model is more sensitive to those low-magnitude spectral changes.

Another obvious advantage of S-CCD is that it is a completely online monitoring algorithm, which can be directly used for near real-time forest monitoring. S-CCD improves several steps of COLD and enables a continuous monitoring in a completely recursive form by using such as the adjusted peek window, recursive temporal RMSE. More importantly, the core technique for S-CCD, the Kalman filter, is a powerful real-time algorithm well known for its high computational efficiency and short-memory requirement. For COLD, limited by its manner for re-constructing the model per observation, it requires reading all images into the system to rebuild harmonic curves for each new observation. Instead, S-CCD just needs to update those parameter files (e.g., states and covariance) once the initialization is finished, which can reduce ~95% of data inputs for monitoring each new observation.

We reported lag-alert relationship curves which is designed to assess timeliness for identifying disturbance events in a near real-time scenario (see Fig. 9). Fig. 12 illustrates an example that S-CCD needs shorter lag time to confirm a change based upon a gypsy-moth-affected pixel. The shorter lag is mainly attributed to the new temporally-adjusted peek window adopted by S-CCD that defines the peek window as calendar days, not a fixed observation number as COLD does. COLD employs a fixed peak window of 12 observations for this case as the median revisit days is 8 days (see Formula S2 in the supplementary material of Zhu

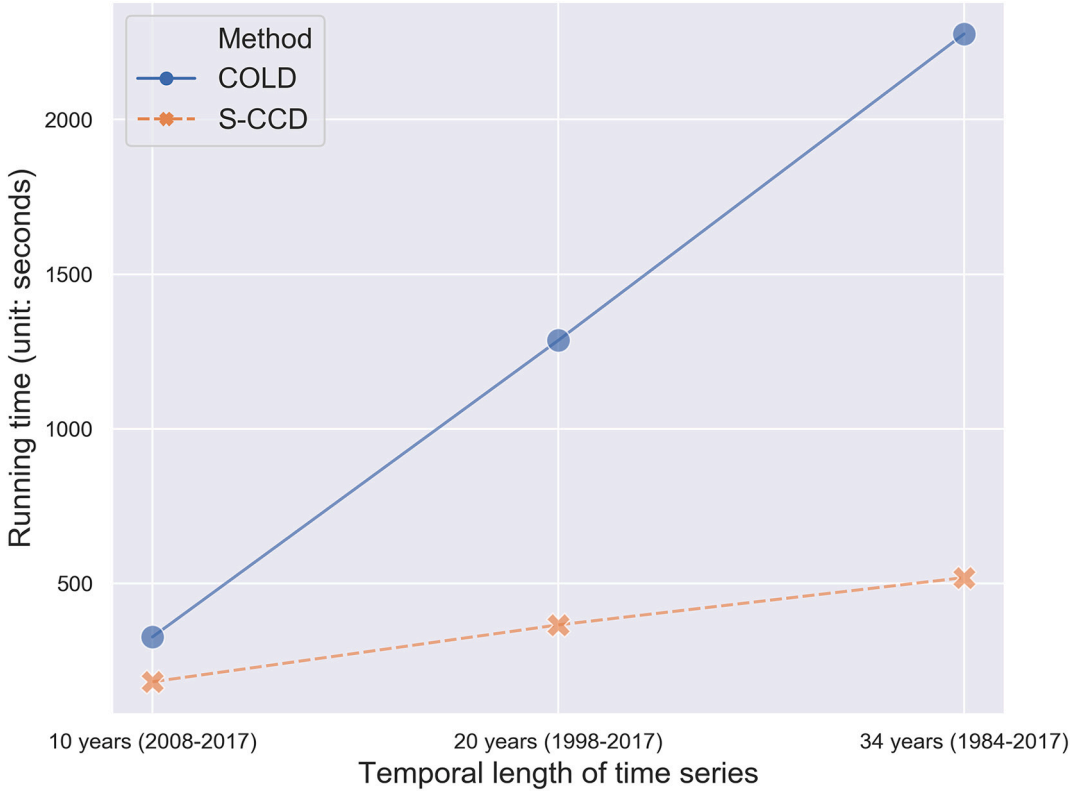

Fig. 11. The result for the efficiency test based on a dummy Landsat ARD scanline (5000 sample pixels). Each time series are pruned as three versions for time series records, that is 10 years (2008–2017), 20 years (1998–2017), 34 years (1984–2017). The result shows that the efficiency of S-CCD was increased as the length of time series increased, and can be up to 4.4 times faster than COLD. The CPU is Intel(R) Core (TM) i7–4790, 3.60GHz.

Table 1
the average RMSE of COLD and S-CCD for each band using 3782 forest samples across the conterminous United States (the bold columns are the two bands that S-CCD has higher RMSE than COLD).

Band	Blue	Green	Red	**NIR**	SWIR1	SWIR2	Thermal
COLD	122.682	117.127	122.473	**273.336**	197.937	151.032	**389.227**
S-CCD	119.061	110.761	118.476	**279.478**	191.518	150.098	**401.061**

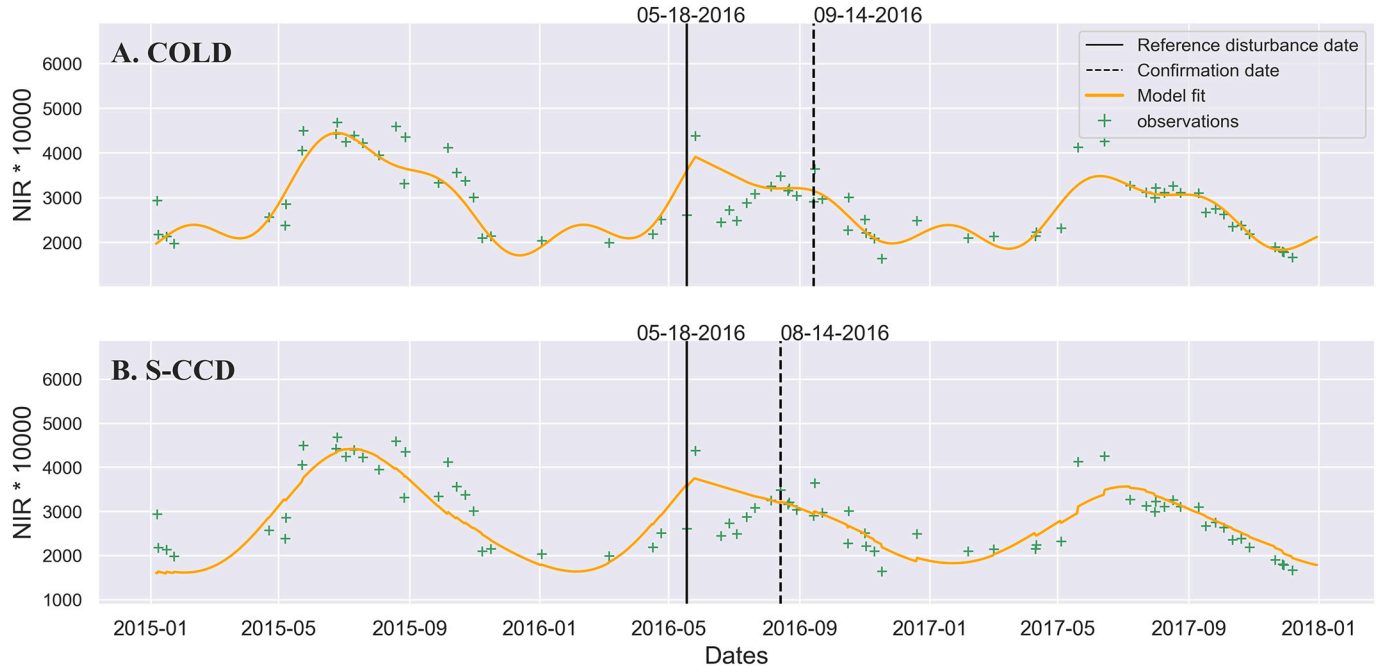

Fig. 12. A gypsy-moth example for COLD and S-CCD detecting breakpoints in a near real-time manner. The black line represents the reference disturbance date; the dash line is the date that this change was confirmed based on consecutive anomaly observations (i.e., peek window). The date difference between the two lines represents 'lag time' when the algorithm is applied to near real-time monitoring. S-CCD shows shorter lag time benefited from its temporally-adjusted peek window defined as a fixed calendar days.

et al. (2020). When the peek window spans over a period of sparse clear observations such as June 2016 in this case, the peek window for COLD has to be extended in order to incorporate enough clear observations. Differently, S-CCD defines the peek window as the minimum width of 80 calendar days, and hence identified the disturbance roughly one month earlier than that of COLD, regardless of temporal density. It is also noteworthy that though S-CCD requires an anomaly peek window of at least 80 days (*min_peek_days*) to confirm a disturbance, the outputted metric of disturbance probability allows for an earlier and more flexible decision-making process: for example, Fig. 10 shows that the pixels homogeneously presented a disturbance probability of 0.5 over 30 days since the initial gypsy moth attack, making it potentially feasible to yield a disturbance alert much earlier than 80 days by applying different probability thresholds.

A possible concern is that S-CCD assumes a consistent structure of time series for trend, annual and semi-annual harmonic items (equal to 6-coefficient harmonic models), while Zhu et al. (2020) suggested using a harmonic model with a maximum coefficient as 8, including trend, annual, semi-annual and trimodal harmonic items (frequency = $^1/_3$ year). As such, we tested adding an additional trimodal cycle component into the presumed time series structure of S-CCD, and found that the best F1 score decreased from 0.795 to 0.706 for S-CCD (see Fig. S4 in the supplementary material). In a harmonic regression, trimodal component can be viewed as an additional modifier to annual and semi-annual curves (Eastman et al., 2009). The state space model adopted a totally different strategy to resolve unexplained variance from annual and semi-annual curves: the state space model assumes that the trend and seasonality states are evolving as time goes by (see Fig. 2B), instead of following a fixed set of harmonic coefficients, thus the unexplained variances can be 'ingested' immediately by changes in structure over time. Another reason might be that we focus on forest disturbance detection for this study, while the trimodal component is often found to be more useful for modeling cropland dynamics.

Admittedly, COLD is designed for detecting/characterizing all types of land disturbances, not limited to forest disturbances. We tested S-CCD against a reference dataset for comprehensive land types, and reached a slightly lower F1 score compared with COLD (0.69 vs 0.71). Our test shows that S-CCD performs less ideal under a highly-fluctuated environment, and is more prone to over-detection due to those ephemeral changes that have a high change magnitude, such as moisture change for grassland/bare land and agricultural rotation. To alleviate this issue, our software package enables users to specify a mask for focused study area, which can exclude the regions where uninterested land change occur and greatly improve processing efficiency as well. Yet, there is still much studies that is needed to analyze characteristics of detected breaks and select breaks only linked to targeted physical processes. Another reason for the unsatisfactory results is that we often have multiple historical data sources to confirm forest disturbances such as the ADS and the LANDFIRE products, but reliable references for the other non-forest land disturbance are lacking. The quality of our non-forest land samples might affect the final accuracy result. Our future work will be directed into 1) modifying S-CCD to accommodate other applications such as agricultural shifts and urban expansion, and 2) tuning the algorithm for the optimal parameters, such as probability threshold and *min_peek_days*, for better detection of targeted change agents and timely warning of land disturbance.

7. Conclusion

We presented an improved time series framework, Stochastic Continuous Change Detection (S-CCD), for near real-time forest disturbance monitoring. The new approach introduces the state space model into the current framework for Continuous Monitoring of Land Disturbance (COLD), to facilitate a near real-time analytics of forest dynamics with a shorter lag time and improve computational efficiency. S-CCD provides an accurate mapping for timing and change magnitude of forest disturbance, and uncovers complex nonlinear dynamics from time series data. Most notably, S-CCD can improve the monitoring for those disturbances that induce subtle spectral changes.

Declaration of Competing Interest

None.

Acknowledgement

We gratefully acknowledge the support of American Society of Photogrammetry and Remote Sensing (ASPRS) William A. Fisher Scholarship and Albert, and Norma and Howard Geller'77 Endowed Research Awards to Su Ye. This research was partially supported by the USGS-NASA Landsat Science Team Program for Toward Near Real-time Monitoring and Characterization of Landsat Surface Change for the Conterminous US (140G0119C0008) to Zhe Zhu. The content of this document does not necessarily represent the views or policies of the Department of the Interior, nor does mention of trade names, commercial products or organizations imply endorsement by the U.S. Government.

Appendix

The system matrices for 'trend+annual+semi-annual' time series structural model are defined by

$$Z = (1, 1, 0, 1, 0) \tag{A1}$$

$$Q = diag\left(\sigma_{\xi}^2, \sigma_{\omega,annual}^2, \sigma_{\omega^*,annual}^2, \sigma_{\omega,semi}^2, \sigma_{\omega^*,semi}^2\right) \tag{A2}$$

$$T = \begin{bmatrix} 1 & 0 & 0 & 0 & 0 \\ 0 & cos\left(\frac{2\pi}{365.25}\right) & sin\left(\frac{2\pi}{365.25}\right) & 0 & 0 \\ 0 & -sin\left(\frac{2\pi}{365.25}\right) & cos\left(\frac{2\pi}{365.25}\right) & 0 & 0 \\ 0 & 0 & 0 & cos\left(\frac{2\pi}{2*365.25}\right) & sin\left(\frac{2\pi}{2*365.25}\right) \\ 0 & 0 & 0 & -sin\left(\frac{2\pi}{2*365.25}\right) & cos\left(\frac{2\pi}{2*365.25}\right) \end{bmatrix} \tag{A3}$$

The Kalman filter recursion for the general Gaussian model of form are

$$v_{t,i} = y_{t,i} - Z\, a_{t,i} \tag{A4}$$

$$F_{t,i} = Z\, P_{t,i} Z^T + H_i \tag{A5}$$

$$K_{t,i} = P_{t,i} Z^T \tag{A6}$$

$$a_{t|t,i} = a_{t,i} + K_{t,i} F_{t,i}^{-1} v_{t,i} \tag{A7}$$

$$a_{t+1,i} = T\, a_{t|t,i} \tag{A8}$$

$$P_{t+1,i} = T\left(P_{t,i} - K_{t,i} K_{t,i}^T F_{t,i}^{-1}\right) T^T + Q_i \tag{A9}$$

Where.

$y_{t,\,i}$: the observation at time t for band i.

$v_{t,\,i}$: the innovation, namely the difference between predicted and actual observations, at time t for band i

Z: the system matrix that determines which items in the state vector are included for the observation

$K_{t,\,i}$: the Kalman gain which is the relative ratio of being assigned to the model update is from the innovation at time t for band i

$P_{t,\,i}$: the covariance matrix at time t for band i

$a_{t|t,\,i}$: the filtered states at time t for band i

$F_{t,\,i}$: the variance of the innovation $v_{t,\,i}$

Q_i: the process noise for band i

H_i: the observational noise for band i

For missing observation, there is no innovation $v_{t,\,i}$. Therefore, the mathematical treatment for state and covariance matrix updates can be simply put as

$$a_{t+1,i} = T\, a_{t|t,i} \tag{A10}$$

$$P_{t+1,i} = T P_{t,i} T^T + Q_i \tag{A11}$$

Appendix A. Supplementary data

Supplementary data to this article can be found online at https://doi.org/10.1016/j.rse.2020.112167.

References

Allen, C.D., Breshears, D.D., McDowell, N.G., 2015. On underestimation of global vulnerability to tree mortality and forest die-off from hotter drought in the Anthropocene. Ecosphere 6, 1–55.

Brockwell, P.J., Davis, R.A., 2013. Introduction to Time Series and Forecasting (Springer Science & Business Media).

Brown, J.F., Tollerud, H.J., Barber, C.P., Zhou, Q., Dwyer, J.L., Vogelmann, J.E., Loveland, T.R., Woodcock, C.E., Stehman, S.V., Zhu, Z., Pengra, B.W., Smith, K., Horton, J.A., Xian, G., Auch, R.F., Sohl, T.L., Sayler, K.L., Gallant, A.L., Zelenak, D., Reker, R.R., Rover, J., 2019. Lessons learned implementing an operational continuous United States national land change monitoring capability: the land change monitoring, assessment, and projection (LCMAP) approach. Remote Sens. Environ. 111356.

Bullock, E.L., Woodcock, C.E., Holden, C.E., 2019. Improved change monitoring using an ensemble of time series algorithms. Remote Sens. Environ. 111165.

Burkett, V.R., Wilcox, D.A., Stottlemyer, R., Barrow, W., Fagre, D., Baron, J., Price, J., Nielsen, J.L., Allen, C.D., Peterson, D.L., Ruggerone, G., Doyle, T., 2005. Nonlinear dynamics in ecosystem response to climatic change: case studies and policy implications. Ecol. Complex. 2, 357–394.

Carlson, A.R., Sibold, J.S., Assal, T.J., Negrón, J.F., 2017. Evidence of compounded disturbance effects on vegetation recovery following high-severity wildfire and spruce beetle outbreak. PLoS One 12, e0181778.

Cohen, W.B., Yang, Z., Stehman, S.V., Schroeder, T.A., Bell, D.M., Masek, J.G., Huang, C., Meigs, G.W., 2016. Forest disturbance across the conterminous United States from 1985–2012: the emerging dominance of forest decline. For. Ecol. Manag. 360, 242–252.

Cohen, W.B., Healey, S.P., Yang, Z., Stehman, S.V., Brewer, C.K., Brooks, E.B., Gorelick, N., Huang, C., Hughes, M.J., Kennedy, R.E., 2017. How similar are forest disturbance maps derived from different Landsat time series algorithms? Forests 8, 98.

Coleman, T.W., Graves, A.D., Heath, Z., Flowers, R.W., Hanavan, R.P., Cluck, D.R., Ryerson, D., 2018. Accuracy of aerial detection surveys for mapping insect and disease disturbances in the United States. For. Ecol. Manag. 430, 321–336.

Curran, L.M., Trigg, S.N., 2006. Sustainability science from space: quantifying forest disturbance and land-use dynamics in the Amazon. In: Proceedings of the National Academy of Sciences of the United States of America, *103*, pp. 12663–12664.

Cyphers, L., Mackes, K., Duda, K., 2019. Timber losses from west fork complex fire in Southwest Colorado. For. Prod. J. 69 (4), 272–277.

Dale, V.H., Joyce, L.A., McNulty, S., Neilson, R.P., Ayres, M.P., Flannigan, M.D., Hanson, P.J., Irland, L.C., Lugo, A.E., Peterson, C.J., 2001. Climate change and forest disturbances. BioScience 51, 723–734.

Davis, M.H.A., Vinter, R.B., 1985. Stochastic models. Stoch. Model. Control 60–99.

Davis, B., Guo, S., Smith, K., 2017. Land Change Monitoring Assessment and Projection (LCMAP) Python Implementation of Continuous Change Detection (pyccd). Department of Interior U.S. Geological Survey.

Durbin, J., Koopman, S.J., 2012. Time Series Analysis by State Space Methods: Second Edition (OUP Oxford).

Dwyer, J., Roy, D., Sauer, B., Jenkerson, C., Zhang, H., Lymburner, L., 2018. Analysis ready data: enabling analysis of the Landsat archive. Remote Sens. 10.

Eastman, J.R., Sangermano, F., Ghimire, B., Zhu, H., Chen, H., Neeti, N., Cai, Y., Machado, E.A., Crema, S.C., 2009. Seasonal trend analysis of image time series. Int. J. Remote Sens. 30, 2721–2726.

Eastman, J.R., Sangermano, F., Machado, E.A., Rogan, J., Anyamba, A., 2013. Global trends in seasonality of normalized difference vegetation index (NDVI), 1982–2011. Remote Sens. 5, 4799–4818.

Hammer, D., Kraft, R., Wheeler, D., 2014. Alerts of forest disturbance from MODIS imagery. Int. J. Appl. Earth Obs. Geoinf. 33, 1–9.

Hansen, M.C., Krylov, A., Tyukavina, A., Potapov, P.V., Turubanova, S., Zutta, B., Ifo, S., Margono, B., Stolle, F., Moore, R., 2016. Humid tropical forest disturbance alerts using Landsat data. Environ. Res. Lett. 11, 034008.

Hart, S.J., Veblen, T.T., 2015. Detection of spruce beetle-induced tree mortality using high-and medium-resolution remotely sensed imagery. Remote Sens. Environ. 168, 134–145.

Helske, J., 2016. KFAS: Exponential Family State Space Models in R. *arXiv [stat.CO]*.

Jamali, S., Jönsson, P., Eklundh, L., Ardö, J., Seaquist, J., 2015. Detecting changes in vegetation trends using time series segmentation. Remote Sens. Environ. 156, 182–195.

Kalman, R.E., 1960. A new approach to linear filtering and prediction problems. Int. J. Eng. Trans. A 82, 35–45.

Kautz, M., Meddens, A.J., Hall, R.J., Arneth, A., 2017. Biotic disturbances in northern hemisphere forests–a synthesis of recent data, uncertainties and implications for forest monitoring and modelling. Glob. Ecol. Biogeogr. 26, 533–552.

Kennedy, R.E., Yang, Z., Cohen, W.B., 2010. Detecting trends in forest disturbance and recovery using yearly Landsat time series: 1. LandTrendr—Temporal segmentation algorithms. Remote Sens. Environ. 114, 2897–2910.

Kennedy, R.E., Andréfouët, S., Cohen, W.B., Gómez, C., Griffiths, P., Hais, M., Healey, S. P., Helmer, E.H., Hostert, P., Lyons, M.B., Others, 2014. Bringing an ecological view of change to Landsat-based remote sensing. Front. Ecol. Environ. 12, 339–346.

Masek, J.G., Huang, C., Wolfe, R., Cohen, W., Hall, F., Kutler, J., Nelson, P., 2008. North American forest disturbance mapped from a decadal Landsat record. Remote Sens. Environ. 112, 2914–2926.

Masek, J.G., Goward, S.N., Kennedy, R.E., Cohen, W.B., Moisen, G.G., Schleeweis, K., Huang, C., 2013. United States Forest disturbance trends observed using Landsat time series. Ecosystems 16, 1087–1104.

Olsson, P.-O., Lindström, J., Eklundh, L., 2016. Near real-time monitoring of insect induced defoliation in subalpine birch forests with MODIS derived NDVI. Remote Sens. Environ. 181, 42–53.

Paritsis, J., Veblen, T.T., 2011. Dendroecological analysis of defoliator outbreaks on Nothofagus pumilio and their relation to climate variability in the Patagonian Andes. Glob. Chang. Biol. 17, 239–253.

Pasquarella, V., Bradley, B., Woodcock, C., 2017. Near-real-time monitoring of insect defoliation using Landsat time series. Forests 8, 275.

Pasquarella, V., Elkinton, J.S., Bradley, B.A., 2018. Extensive gypsy moth defoliation in southern New England characterized using Landsat satellite observations. Biol. Invasions 20, 3047–3053.

Pasricha, G.K., 2006. Kalman Filter and its Economic Applications.

Pechony, O., Shindell, D.T., 2010. Driving forces of global wildfires over the past millennium and the forthcoming century. In: Proceedings of the National Academy of Sciences, *107*, pp. 19167–19170.

Preisler, H.K., Hicke, J.A., Ager, A.A., Hayes, J.L., 2012. Climate and weather influences on spatial temporal patterns of mountain pine beetle populations in Washington and Oregon. Ecology 93, 2421–2434.

Reymondin, L., Jarvis, A., Perez-Uribe, A., Touval, J., Argote, K., Rebetez, J., Guevara, E., Mulligan, M., 2012. A Methodology for near Real-Time Monitoring of Habitat Change at Continental Scales Using MODIS-NDVI and TRMM (Submitted Remote Sensing of Environment).

Rogan, J., Mietkiewicz, N., 2015. Land cover change detection. In: Thenkabail, P.S. (Ed.), Land Resources Monitoring, Modeling, and Mapping with Remote Sensing, pp. 579–603.

Schmidt, S.F., 1981. The Kalman filter - its recognition and development for aerospace applications. J. Guid. Control. Dyn. 4, 4–7.

Sedano, F., Kempeneers, P., Hurtt, G., 2014. A Kalman filter-based method to generate continuous time series of medium-resolution NDVI images. Remote Sens. 6, 12381–12408.

Seidl, R., Thom, D., Kautz, M., Martin-Benito, D., Peltoniemi, M., Vacchiano, G., Wild, J., Ascoli, D., Petr, M., Honkaniemi, J., 2017. Forest disturbances under climate change. Nat. Clim. Chang. 7, 395–402.

Tang, X., Bullock, E.L., Olofsson, P., Estel, S., Woodcock, C.E., 2019. Near real-time monitoring of tropical forest disturbance: new algorithms and assessment framework. Remote Sens. Environ. 224, 202–218.

Tang, X., Bullock, E.L., Olofsson, P., Woodcock, C.E., 2020. Can VIIRS continue the legacy of MODIS for near real-time monitoring of tropical forest disturbance? Remote Sens. Environ. 249, 112024.

Townsend, P.A., Eshleman, K.N., others, 2004. Remote sensing of gypsy moth defoliation to assess variations in stream nitrogen concentrations. Ecological Applications 14 (2), 504–516.

Turner, M.G., Baker, W.L., Peterson, C.J., Peet, R.K., 1998. Factors influencing succession: lessons from large, infrequent natural disturbances. Ecosystems 1, 511–523.

Verbesselt, J., Hyndman, R., Newnham, G., Culvenor, D., 2010a. Detecting trend and seasonal changes in satellite image time series. Remote Sens. Environ. 114, 106–115.

Verbesselt, J., Hyndman, R., Zeileis, A., Culvenor, D., 2010b. Phenological change detection while accounting for abrupt and gradual trends in satellite image time series. Remote Sens. Environ. 114, 2970–2980.

Verbesselt, J., Zeileis, A., Herold, M., 2012. Near real-time disturbance detection using satellite image time series. Remote Sens. Environ. 123, 98–108.

Verdin, K.L., Dupree, J.A., Stevens, M.R., 2013. Postwildfire Debris-Flow Hazard Assessment of the Area Burned by the 2013 West Fork Fire Complex, Southwestern Colorado. US Department of the Interior, US Geological Survey.

Vicente-Guijalba, F., Martinez-Marin, T., Lopez-Sanchez, J.M., 2014. Crop phenology estimation using a multitemporal model and a Kalman filtering strategy. IEEE Geosci. Remote Sens. Lett. 11, 1081–1085.

Vogelmann, J.E., Gallant, A.L., Shi, H., Zhu, Z., 2016. Perspectives on monitoring gradual change across the continuity of Landsat sensors using time-series data. Remote Sens. Environ. 185, 258–270.

Walters, S.P., Schneider, N.J., Guthrie, J.D., 2011. Geospatial Multi-Agency Coordination (GeoMAC) Wildland Fire Perimeters, 2008 (Data Series).

Westerling, A.L., 2016. Increasing western US forest wildfire activity: sensitivity to changes in the timing of spring. Philos. Trans. R. Soc. B 371, 20150178.

Woodcock, C.E., Allen, R., Anderson, M., Belward, A., Bindschadler, R., Cohen, W., Gao, F., Goward, S.N., Helder, D., Helmer, E., 2008. Free access to Landsat imagery. Science 320 (1011–1011).

Ye, S., Rogan, J., Sangermano, F., 2018. Monitoring rubber plantation expansion using Landsat data time series and a Shapelet-based approach. ISPRS J. Photogramm. Remote Sens. 136, 134–143.
Zhao, K., Wulder, M.A., Hu, T., Bright, R., Wu, Q., Qin, H., Li, Y., Toman, E., Mallick, B., Zhang, X., Brown, M., 2019. Detecting change-point, trend, and seasonality in satellite time series data to track abrupt changes and nonlinear dynamics: a Bayesian ensemble algorithm. Remote Sens. Environ. 232, 111181.
Zhu, Z., 2017. Change detection using landsat time series: a review of frequencies, preprocessing, algorithms, and applications. ISPRS J. Photogramm. Remote Sens. 130, 370–384.
Zhu, Z., 2019. Science of Landsat analysis ready data. Remote Sens. 11, 2166.
Zhu, Z., Woodcock, C.E., 2012. Object-based cloud and cloud shadow detection in Landsat imagery. Remote Sens. Environ. 118, 83–94.
Zhu, Z., Woodcock, C.E., 2014a. Automated cloud, cloud shadow, and snow detection in multitemporal Landsat data: an algorithm designed specifically for monitoring land cover change. Remote Sens. Environ. 152, 217–234.
Zhu, Z., Woodcock, C.E., 2014b. Continuous change detection and classification of land cover using all available Landsat data. Remote Sens. Environ. 144, 152–171.
Zhu, Z., Woodcock, C.E., Olofsson, P., 2012. Continuous monitoring of forest disturbance using all available Landsat imagery. Remote Sens. Environ. 122, 75–91.
Zhu, Z., Woodcock, C.E., Holden, C., Yang, Z., 2015. Generating synthetic Landsat images based on all available Landsat data: predicting Landsat surface reflectance at any given time. Remote Sens. Environ. 162, 67–83.
Zhu, Z., Zhang, J., Yang, Z., Aljaddani, A.H., Cohen, W.B., Qiu, S., Zhou, C., 2020. Continuous monitoring of land disturbance based on Landsat time series. Remote Sens. Environ. 238, 111116.